

OPTIMIZED AND INTEGRATED ALIGNMENT SYSTEM FOR FUNCTIONAL
PROTON RADIOSURGERY

A Thesis
Presented to the
Faculty of
California State University,
San Bernardino

In Partial Fulfillment
of the Requirements for the Degree
Master of Science
in
Computer Science

by
Fadi Easa Shihadeh
June 2007

OPTIMIZED AND INTEGRATED ALIGNMENT SYSTEM FOR FUNCTIONAL
PROTON RADIOSURGERY

A Thesis
Presented to the
Faculty of
California State University,
San Bernardino

by
Fadi Easa Shihadeh

June 2007

Approved by:

Dr. Keith Evan Schubert, Advisor,
Computer Science

Date

Dr. Reinhard Schulte

Dr. Arturo Concepcion

Dr. Ernesto Gomez

© 2007 Fadi Easa Shihadeh

ABSTRACT

Radiosurgery is a non-invasive treatment technique applying focused radiation beams. It requires high geometric accuracy as misalignment can cause damage to the surrounding healthy tissues and loss of the therapeutic effect. One promising technique to ensure sub-millimeter alignment accuracy of the radiation beam is to optically monitor the position of the beam axis relative to a frame firmly attached to the patient's skull using an optical alignment system. The optical alignment method requires an Optical Localization System (OLS) and a marker system visible to the OLS in order to derive three-dimensional coordinate transforms needed to align the proton beam axis to its stereotactic target. Once the target and the proton beam are defined in the same coordinate system, an alignment control system can be used to align the beam to the target. In this thesis work, a system for proton beam alignment was studied and optimized in many of its functional areas. The resulting system was named Positioning Alignment Control System (PACS). The PACS system is an integrated and efficient system as a result of the work done on it in the course of this thesis work.

ACKNOWLEDGEMENTS

I want to express my deepest appreciation and thanks to Dr. Keith Schubert and Dr. Reinhard Schulte. Dr. Schubert introduced me to professional level computer science and Dr. Schulte introduced me to professional level research and science. Without their dedicated support for many long hours I would not have accomplished this piece of work.

I would like to also thank many people who helped me through my education and research including: Dr. Arturo Concepcion for his continued advice and leadership, Dr. Ernesto Gomez for his listening and guidance, Dr. Kay Zemoudeh for making me a much better programmer, and all the faculty of California State University San Bernardino for making this school a place for excellence in education.

TABLE OF CONTENTS

<i>Abstract</i>	iii
<i>Acknowledgements</i>	iv
<i>List of Tables</i>	ix
<i>List of Figures</i>	x
<i>1. Introduction</i>	1
1.1 Background	1
1.1.1 Protons in Radiation Therapy and Radiosurgery	1
1.1.2 Radiosurgery with Protons	3
1.1.3 Patient Alignment and Verification Issues	5
1.2 Significance	6
1.2.1 Potential Applications and Benefits of Precision Proton Beams	6
1.3 Purpose	8
1.3.1 Previous Work	8
1.3.2 Objectives of this Thesis	8
1.3.3 Thesis Overview	11
<i>2. System Description</i>	13
2.1 Introduction	13
2.2 Vicon Cameras	13

2.3	Leksell Halo System	13
2.4	Marker Systems	14
2.5	Supporting Components	16
2.5.1	The Micro-Stage	16
2.5.2	Micro-Stage Cart	16
2.5.3	L-Frame and Calibration Wand	18
2.6	PACS System Setup	19
2.7	PACS System Functional Description	21
2.8	Operation of the Alignment Control System	23
2.8.1	Stereotactic Transformation Algorithm	25
3.	<i>OLS System Characterization</i>	26
3.1	Introduction	26
3.2	Purpose	26
3.3	Terminology	27
3.4	Independent Experimental Factors	28
3.4.1	Camera Configuration	28
3.4.2	Calibration Technique	29
3.4.3	Experimental Design and Data Analysis	30
3.5	Results	31
3.5.1	Calibration Factors	31
3.5.2	Distance Error	32
3.5.3	Shift Error	34
3.6	Discussion and Conclusions	36
3.6.1	Summary of Findings	38
4.	<i>Improved Caddy Design</i>	40
4.1	Purpose	40

4.2	Theoretical Considerations	40
4.2.1	The Old Caddy Design	40
4.2.2	Requirements for a New Caddy	41
4.3	Engineering the New Caddy	42
4.3.1	Current Status of Design	42
4.3.2	The Design Process	42
4.4	Experimental Verification of New Design and Selection of Best Marker Triangles	43
4.4.1	Purpose	43
4.4.2	Triangle Study Hypothesis	44
4.4.3	Method Outline	44
4.4.4	Results	45
4.4.5	Conclusions	46
4.5	Summary of Improvements	48
5.	<i>Refinement of the Stereotactic Transformation Algorithm</i>	49
5.1	Purpose	49
5.2	Triangles used in the Transformation	49
5.3	Averaging of Rotation Matrices	49
5.4	Summary of Improvements	50
6.	<i>Software Improvements and Development</i>	51
6.1	Introduction	51
6.2	Camera Orientation Software	51
6.3	Improving the Data Acquisition Process	52
6.4	Improving the Image Processing Software	53
6.5	Implementation of a GUI based Alignment Package	54
6.6	Summary of Software Improvements and Developments	57

7. <i>Conclusions and Future Direction</i>	58
7.1 Conclusions	58
7.1.1 Vicon Camera Performance	58
7.1.2 The Improved Caddy	59
7.1.3 Rotational Transformation	60
7.2 Future Direction	60
7.2.1 Global System Performance	60
7.2.2 Propagation of Error	61
7.2.3 Marker Systems	61
7.2.4 Vicon Cameras	61
7.2.5 The Cross Marker System	62
<i>Appendix A: STEREOTACTIC TRANSFORMATIONS FOR FUNCTIONAL PROTON RADIOSURGERY</i>	63
1.1 Introduction	64
1.2 Mathematical Method to Compute the Transformation Between Local and Global Coordinate Systems	64
1.2.1 Outline of the Transformation Strategy	64
1.2.2 Rotation of a Vector About a Non-collinear Vector	66
1.3 Derivation of the Matrix M_A	67
1.3.1 Derivation of the Matrix \mathbf{M}_B and the Vector \mathbf{t}	68
1.4 Quality Check of the Transformation	69
<i>References</i>	72

LIST OF TABLES

3.1	Calibration Parameters	32
3.2	Mean Distance Errors	33
3.3	Mean Shift Errors	35

LIST OF FIGURES

1.1	Dosage Profile of a High Energy Proton Beam vs. a Photon Beam. Adapted from [12]	3
1.2	Relative Dose of a 6MV Linac vs. Proton Beams with Four Different Energies. Courtesy of Massachusetts General Hospital	4
2.1	Three Vicon Cameras in the Standard Configuration	14
2.2	Leksell Halo	15
2.3	Harvey Mudd Marker Caddy Design	16
2.4	New Caddy Design	17
2.5	Cone Cross Marker System	17
2.6	Caddy Mounted on the Micro Stage with Bracket	18
2.7	Micro Stage Mounted on Specialized Cart	19
2.8	Experimental Setup with Main Hardware Components of the PACS. .	20
2.9	Marker Systems in Gantry Setup	20
2.10	Marker Caddy, Fine Alignment Stage and Holding Bracket in Gantry	21
2.11	PACS Deployment Diagram	22
2.12	Interaction Between the PACS System and Other Components	23
2.13	Flow Chart of the PACS System	24
3.1	Estimated Standard Deviation Components and 95% Confidence In- tervals of the Distance Measurement.	34

3.2	Estimated Standard Deviation Components and 95% Confidence Intervals of the Shift Measurement. Negative Variances were Truncated to Zero.	36
4.1	Minimum Angle vs. Average Transformation RMS	45
4.2	Minimum Angle vs. Log(RMS)	46
4.3	Triangle Area vs. Average RMS	47
4.4	Triangle Area vs. Log(RMS)	47
6.1	Camera Position and Orientation Software.	52
6.2	Screen Capture for the Image Processing GUI.	55
6.3	Screen Capture for the Alignment GUI.	56
1.1	Conceptual View of the Two Marker Sets in the Local and Global Reference Systems [8]	65
1.2	(a) Definition of the Normal Vectors \mathbf{n}^l and \mathbf{n}^g , and (b) Rotation Performed by Matrix \mathbf{M}_A . [8]	67
1.3	(a) Definition of the Normal Vectors \mathbf{u}^l and \mathbf{u}^g , and (b) Rotation Performed by Matrix \mathbf{M}_B . [8]	68

1. INTRODUCTION

1.1 *Background*

1.1.1 *Protons in Radiation Therapy and Radiosurgery*

Protons are one of many forms of radiation used in therapy. Proton therapy works by aiming accelerated protons onto the target, usually a tumor. These particles damage the DNA of targeted cells and, thereby, cause them to die. Cancer cells have a higher rate of division than healthy cells and a much reduced ability to repair their DNA damage and thus proton bombardment causes them to die.

Radiosurgery is a medical procedure which allows non-invasive brain surgery by means of a precise spatial delivery of radiation. During radiosurgery, ionizing radiation beams are focused on intracranial targets, such as tumors or brain tissue affected by functional disorders such as Parkinson's disease. Other than the fact that this technique does not require a surgical opening of the skull, operating on deep brain regions is often difficult because of the many veins and arteries and other critical structures that could be damaged enroute to the target.

Wilson Suggests the Clinical Use of Protons

Robert R. Wilson [10] was an American physicist who was a group leader of the Manhattan Project, a sculptor, and an architect of Fermi National Laboratory (Fermilab), was the first to suggest the use of protons for radiotherapy in 1946. The depth of penetration of a proton beam in matter is finite and this depth is a function of the electron density of the material being irradiated [12] and can be adjusted by choosing the right proton energy. The capability to control proton beams and the

ability to minimize the effect to healthy tissue made protons an attractive solution to many of the shortcomings of photon and neutron therapy; but only after 3-D imaging modalities such as Computed Tomography (CT) and Magnetic Resonance Imaging (MRI) became available in the 1970s and 1980s, protons started to be used more commonly. Today, Wilson's ideas have been adopted by a wide community of radiation oncologists and a great momentum in the field of proton based therapy has begun recently.

The Qualities of Proton Beams that Make them Superior to Photon Beams

As protons do not scatter much in tissue, there is little lateral dispersion; the beam stays focused on the tumor shape without much lateral damage to surrounding tissue. All protons of a given energy have a certain range; no proton penetrates beyond that distance. Furthermore, the dose to tissue is maximum just over the last few millimeters of the particles range, this maximum is called the Bragg peak. This depth depends on the energy to which the particles are accelerated by the proton accelerator. It is therefore possible to focus the cell damage due to the proton beam at the very depth in the tissues where the tumor is situated. By spreading out the Bragg peak to smaller penetration depths using a spinning modulator wheel, tumors larger than the narrow Bragg peak can be covered. All tissues situated before the spread-out Bragg peak receive reduced dose, and tissues situated after the peak receive none.

On the other hand, the range of X-rays or gamma rays (energetic photons) is, in principle, infinite as some of them can penetrate without being scattered or absorbed. Thus, the dose of a photon beam decreases exponentially with respect to depth.

Figure 1.1 shows the dose profile of a photon beam vs. a proton beam. From the figure we can quickly appreciate the implications of beam penetration control. The colored areas in the figure represent the area that will receive unwanted dose due to the physical properties of photons: their infinite range and the fact that the maximum dose is not in the target. Unwanted dose to healthy tissue increases the rate

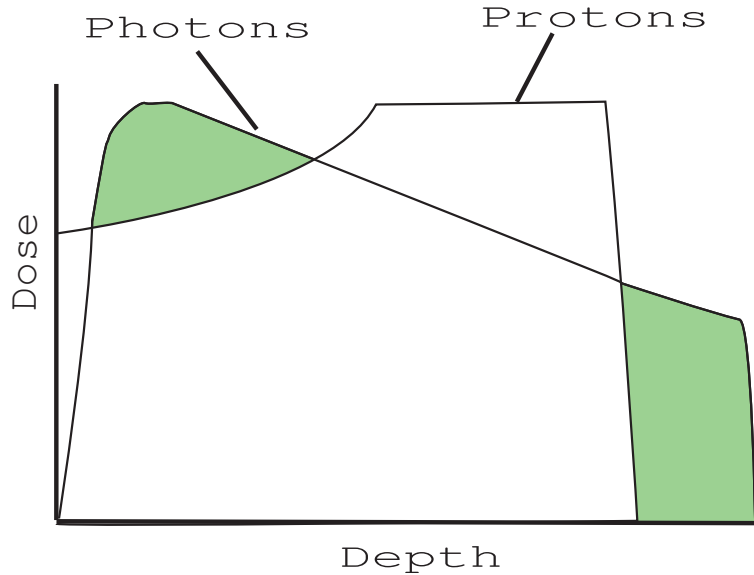


Fig. 1.1: Dosage Profile of a High Energy Proton Beam vs. a Photon Beam. Adapted from [12]

and severity of treatment-related effects. Protons spare normal tissues to a greater degree. The dose fall-off to zero dose occurs just after the maximum energy disposal, which is the Bragg peak, and much lower dose is deposited in front of the target compared to a photon beam. These properties make protons the preferred form of radiation for radiotherapy and radiosurgery.

Figure 1.2 displays measured dose profiles of proton beams with different initial energies and a photon beam of 6 MeV produced by a linear accelerator (Linac) in water as a function of penetration depth. This illustrates the capability of controlling the depth of a proton by choosing the right initial energy. Conversely, a photon beam of higher or lower initial energy will deliver either higher or lower dose at a given depth but will never stop at any depth.

1.1.2 Radiosurgery with Protons

The term radiosurgery was first used by the famous Swedish neurosurgeon Lark Leksell. In his 1951 publication [6], he suggested to converge multiple narrow radiation beams from different directions to create regions of focal destruction in diseased sites

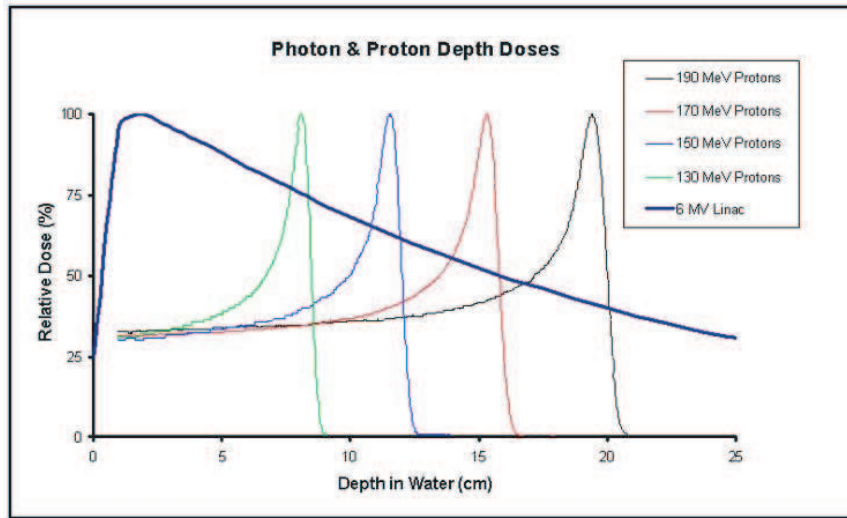


Fig. 1.2: Relative Dose of a 6MV Linac vs. Proton Beams with Four Different Energies. Courtesy of Massachusetts General Hospital

of the brain. Leksell wanted to use this technique, called functional radiosurgery, to treat functional brain disorders such as Parkinson’s disease, a neurological disease that affects millions of elderly people in the U.S.

Dr. Leksell had initially planned to do functional radiosurgery with protons [6] but then backed off and developed the Gamma knife; an instrument for radiosurgery that employs 201 collimated radioactive cobalt sources. The reasons for this were probably three-fold: first, protons were not generally available in hospitals at that time; second, it was quite difficult to accurately place a proton Bragg peak without guidance from modern imaging techniques such as CT and MRI; and third, the lesions created by a proton Bragg peak were not small enough for the purpose of functional lesioning, and proton energies sufficiently high to create sharp shoot-through beams were not available to him.

During the late 1950s, Dr. William Sweet, a leading neurosurgeon at the Massachusetts General Hospital in Boston also became quite interested in the use of protons for radiosurgery. He started a collaboration with a group of physicists at the Harvard cyclotron and together with Dr. Raymond Kjellberg from the MGH implemented a radiosurgery treatment program for tumors of the pituitary gland

using the proton Bragg peak of the 160 MeV Harvard Cyclotron. This program treated several thousand patients for the next 30 years. Dr. Kjellberg, in collaboration with the Harvard cyclotron group also developed a proton radiosurgery program for arteriovenous malformations (AVM), using a similar technique previously developed by Dr. Leksell for the Gamma Knife.

Another milestone in proton therapy and proton radiosurgery was with the opening of the first hospital-based proton treatment center in Loma Linda, CA in 1990. This distinguished center provided, for the first time, proton gantries that can deliver the beam from any angle in a vertical plane. The Loma Linda facility uses a proton synchrotron that can accelerate protons up to energies of 250 MeV, which is sufficient to penetrate a human head if needed.

The physicians at Loma Linda used the techniques previously developed by the group at MGH and the Harvard cyclotron to treat tumors at the base of the skull, but also developed many new techniques to treat other tumors at many different anatomical sites. In 1993, a radiosurgery treatment program for large AVMs was started. A few years later the physicists and physicians developed treatment techniques for tumors and AVMs in the 1-3 cm range using radiosurgical techniques.

Since 1999, a team of physicians and physicists in the Department of Radiation Medicine at LLUMC has been actively involved in developing the capability of performing functional lesioning with protons that can penetrate the skull. The advantage of this technique is that these protons have minimal side scatter and, therefore, very small lesions (1-3 mm) can be created, which would not be possible with the Bragg peak. This thesis work is a derivative of that LLUMC effort.

1.1.3 Patient Alignment and Verification Issues

High radiation doses can be very effective but lead to severe side effects when not placed accurately. Functional proton radiosurgery techniques place very high demands for the accuracy of the patient alignment with respect to the proton beam isocenter. The isocenter is the point where all proton beam axes intersect.

Before a proton treatment takes place, the beam direction and dose distribution are carefully planned and studied by dosimetrists and radiation oncologists. The definition of the target boundaries, or the location of a lesion for functional radiosurgery depends heavily on the accuracy of the imaging procedures that are performed as part of the planning process.

Once the anatomical target point has been localized with CT and/or MRI, it needs to be aligned to the proton beam. This can be accomplished in many different ways, but in stereotactic procedures it is customary to give the target point 3D coordinates in a reference system that is rigidly attached to the patient's skull. The proton treatment isocenter is then aligned to the stereotactic reference system using planar room lasers that intersect at the isocenter.

Relying only on laser localization of the proton isocenter is not sufficient for verification of the correct target position. Additional means for verification must be developed. For current radiosurgery procedures for tumors and AVMs in the 1-3 cm range, the LLUMC team uses orthogonal X-ray films that project small screws implanted into the patient's skull as reference markers with known coordinates. This method, providing accuracy and reproducibility of target-to-isocenter alignment of the order of 1-2 mm is not adequate for functional proton radiosurgery procedures.

Developing better ways to provide alignment and verification with sub-millimeter accuracy is the subject of this thesis and the methods used will be explained in much detail in the subsequent sections.

1.2 Significance

1.2.1 Potential Applications and Benefits of Precision Proton Beams

The work of this thesis contributes to the development of the capability to perform lesioning, i.e., creating small focal lesions, in the brain of animals or humans. This has many potential applications for research and patient treatment.

Proton lesioning can be used, for example, in experimental studies of the animal brain. Creating small lesions in the brain of animals has had a long tradition

among neuroscientists, and with high-resolution image guidance and protons this can be done without having to open the skull of the animal.

A more recent development requiring animal brain lesioning is to bridge interrupted neuro-circuitry in the brain with so-called neuro-silicon hybrid chips [1]. There are several research teams in the U.S. and Europe that are exploring this possibility, among them Dr. Ted Berger at the University of Southern California [3]. The goal is to build artificial neural networks that replace the input of lost brain cells to other cells. Imagine a small chip implanted into a rat brain that registers input and output neural signals in a certain location under many different circumstances and stores these patterns. Next, one would create a small lesion in the brain at a selected location, for example with a well-defined proton beam, that would destroy the previously recorded brain cells. The electronic neuroprosthesis would then replace those cells and provide the original function.

The main clinical indication for functional proton radiosurgery at LLUMC will be Trigeminal Neuralgia (TN), which is a common facial pain disorder related to a malfunction of the fifth cranial nerve (the trigeminus). TN is considered to be one of the most painful clinical conditions with attacks of stabbing facial pain. The origin of TN is a compression of the trigeminal nerve root, usually within a few millimeters of entry into the brain stem. Existing treatment modalities for the management of TN include medical treatment (drug therapy), open or percutaneous surgery, and gamma-knife or linac radiosurgery. Functional radiosurgery with the Gamma knife has been established as an alternative treatment for patients who do not respond to optimal medical management and are not considered candidates for surgical intervention.

Performing lesioning for TN will be a good indication for proton functional radiosurgery as the brain stem can be optimally spared. Gamma knife and linac radiosurgery for TN has been performed with 4 mm collimators and the rate of neurological side effects has been between 7% and 14% [2, 5].

1.3 Purpose

1.3.1 Previous Work

Previous to this body of work, two students from California State University San Bernardino, initiated two different efforts in the course of their thesis work. Before the CSUSB students, a team at Harvey Mudd College in Claremont California, started the effort in a project named “Sequential Alignment and Positioning Verification System”. The Harvey Mudd team did a study to determine the requirements needed to produce the SAPVS system which is a system for optical based alignment of proton beams for functional radiosurgery. The HMC team determined that the Vicon Cameras (Optical) option was the best option available within the different criteria they examined. The HMC team also designed the basic control algorithm and the initial caddy marker system required for optical positioning.

The CSUSB students inherited the SAPVS system and worked on it to improve different aspects of the system including designing the transformation mathematics and improving the performance of the camera system. Many of the areas of the system were implemented in a prototype fashion, thus leaving many areas for work and improvement for this body of work. The improvements done in this thesis to the many aspects of the SAPVS system are previewed in the thesis overview section 1.3.3.

1.3.2 Objectives of this Thesis

This thesis has many objectives. The specific objective of this thesis is to improve on the transformation algorithm in order to achieve the highest accuracy possible. In order to improve the system accuracy, every component of the system was examined and modified to reach a high level of stability and repeatable level of accuracy. The general objectives of the thesis are previewed in the following sub sections.

The Vicon Plug-In

The previous SAPVS system had very limited capability in retrieving data from the OLS system (refer to section 2.2) and formatting it in a usable fashion. The limitation was that the available plug-in could not be used on different marker configurations without first modifying and rebuilding it. In this thesis work, a fully functional plug-in was developed that can handle up to 30 markers and multiple simultaneous captured objects automatically.

Optimal Camera Configuration

The camera configuration (camera positions and orientation towards the markers) could have an effect on the residual error of the cameras. It was believed so far, that an equilateral configuration is a good solution, but other configurations have not been tested. In this thesis work, we studied multiple configurations ranging from theoretically optimal configurations to those we can actually implement in a LLUMC gantry.

GUI Based Alignment and Verification Suite

To complete a successful transformation, we need to capture data and then process it. The plug-in mentioned above will take care of the data capture whereas a new GUI-based solution was developed to aid the user of the system to perform all the necessary calculations in a quick and integrated manner. To achieve this GUI level integrated functionality, text-based MATLAB programs were developed and then converted gradually into a compiled GUI MATLAB program.

Optimize the Mathematical Procedure

The current set of mathematic equations developed to achieve the alignment was reviewed, sources of numerical instability and errors were identified and corrected. As part of the mathematical procedure, triangles need to be selected to calculate the transformation from the global coordinate system to the local coordinate system or

vice versa. These triangles can be of different size and quality. The area of the triangle and the smallest angle in that triangle could be significant factors in the transformation method. Selecting a triangle with certain features could lead to substantial errors in the transformation process. The triangles selected must be ones that minimize the residual error of the transformation. The heart of this thesis study is to optimize the triangle selection and show its direct effect on the final residual error of the transformation process.

GUI Based Image Processing System

Previously, a crude image processing system for testing the performance of the SAPVS was developed by previous students working on this project. In the context of this work, a fully functional GUI-based program was developed. The purpose of this program is to take as input the raw image of a target marker and a laser beam, representing the proton beam, and process it to tell the user how far the beam axis is from the target (residual error).

Optimize Camera Alignment

The position and orientation of the cameras are considered to be variables influencing the system error. Several camera configurations were studied in order to determine the relationship between camera configuration and the system error. The OLS characterization study reported on the difference between two most likely to be used camera configurations, This study is included in chapter 3.

Design and Justify Design of New Caddy

It was known to the team conducting this body of research that the current caddy (developed by Harvey Mudd College team) has design flaws including the fact that typically only 6 out of the 23 markers on it are visible simultaneously by the three cameras. A new set of design goals was developed and a new caddy was produced to

fulfill these design goals. The full description of the design process can be found in chapter 4.

Calibration Method

In previous work, especially in the thesis work of Mr. Mahesh Neupane [9], it was shown that the calibration pattern could affect the overall camera residual errors. Some aspects of this work still needed further exploration, especially the effect of a calibration pattern on the residual error of marker positions. In this thesis work, a systematic study of different calibration patterns was done and the results of that study are explained in chapter 3.

Integrated System

All the systems and technologies developed for the SAVPS had been developed disparately and required a great deal of tedious hand work to process the data and produce a valid transformation. In this thesis, a major part of the work was to automate the data capture, processing, transformation, alignment and verification process such that it requires minimum user interaction. This was a crucial step needed to prepare the system for its clinical application. To achieve this integration level, a modular system will be developed such that each module is independent and only requires a few user interactions to achieve its task. Most software was developed in GUI user friendly format and documented in code and with manuals. The full description of the software developed can be found in chapter 6.

1.3.3 Thesis Overview

This thesis is divided into seven chapters. Chapter 1 introduces the topics of radiation therapy and radiosurgery. The difference between protons and photons is described because photon radiosurgery is the modality that is closest to to proton radiosurgery.

Chapter 2 describes the tools and software used in the Positioning Alignment Control System (PACS). The description of each of the tools is accompanied with a diagram showing the module. The interaction between the different modules is also described and shown in different flow charts and deployment diagrams.

Chapter 3 reports on the statistical analysis and the performance of the PACS system. Different studies were developed in order to quantify the precision and the accuracy of the designed system. The summary of the results are found with a discussion on the experimental conditions and factors.

Chapter 4 explores the work done in improving the marker caddy system. The flaws of the older marker system are described as well as the design process for the new marker system. Lessons learned from the caddy design process are mentioned. The newly designed caddy was studied with respect to the accuracy of the transformations done using it. The results of the triangle based transformation study are explained as well as the best triangle selection process.

Chapter 5 explores the work done to improve the mathematical methods and algorithms used for the transformation process. The transformation software inherited for this work is outlined. The summary of the improvements done on the software will be described and important parts of the code will be listed in pseudocode for better understanding.

Chapter 6 describes in more detail the many improvements done on the software aspect of the system. In the course of this work, many software packages were designed and implemented; these software tools are detailed in that chapter.

Finally, chapter 7 contains the conclusions derived and the future direction for this body of work. Conclusions found for each major component are explained and directions on further improvements are found.

2. SYSTEM DESCRIPTION

2.1 Introduction

In the background section we mentioned the use of the “Sequential Alignment and Positioning Verification System” (SAPVS). The inherited SAPVS system was later dubbed Positioning and Alignment Control System “PACS”. In the following few sections, the components that make the PACS System will be described. The components include: A Camera system, a marker system and a host of support items.

2.2 Vicon Cameras

The Camera system (fig 2.1) is the main Optical Localization System (OLS) used to determine the location of a set of retro-reflective ¹ markers.

The cameras are manufactured by Vicon. With three cameras, a high level of measurement accuracy can be achieved (sub-millimeter accuracy). The cameras capture images of the markers and after running a triangulation algorithm, the data station attached to the cameras produces an output consisting of a C3D file. The C3D file is an industry standard for files containing marker trajectories. In the context of this thesis work, a Vicon Workstation Plug-in was written to extract the coordinates of the markers in the Vicon coordinate system.

2.3 Leksell Halo System

The Leksell Halo system (fig 2.2) is the device used to define the stereotactic coordinate system shared by the marker system and the imaging devices used to

¹ A retro-reflective marker returns light directly back to the light source thus it is highly visible to a camera projecting a signal on it.



Fig. 2.1: Three Vicon Cameras in the Standard Configuration

localize the target.

The official name of the halo is “Leksell G frame” and it is made by Elekta Instruments, a company in Stockholm, Sweden. This halo system is machined with high precision and provides a reliable stereotactic reference system that is used in the medical industry. By looking at figure 2.4 we can see how the marker system (caddy in this case) attaches to the halo to establish a coordinate system for the markers.

2.4 Marker Systems

In order to optically position an object, two specialized marker systems must be used. One marker system (referred to as caddy) must be fixed to the target containing object (an example is a human or animal head). Another marker system (referred to as cross) must be attached to the proton delivery cone in order to identify

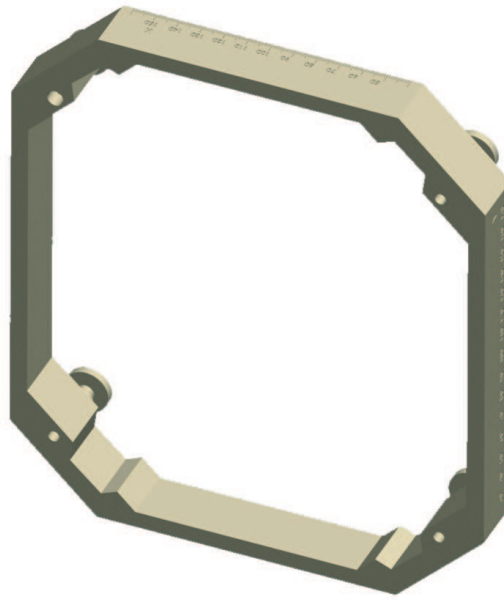


Fig. 2.2: Leksell Halo

the location of the proton beam in the camera system.

The markers are essentially ceramic or plastic spheres covered with a retro-reflective material. Since these markers are made from somewhat fragile materials, one must be careful handling them and placing them in view of the cameras. In previous work, a marker caddy (fig 2.3) was designed by a team of students and faculty at Harvey Mudd College in Claremont, California. In the scope of this thesis work, a need for a new and improved marker caddy was identified and addressed. The newer version of the caddy can be found in figure 2.4.

The difference between the new and old design will be further explained in chapter 4. The design for the cross marker system can also be found in figure 2.5.

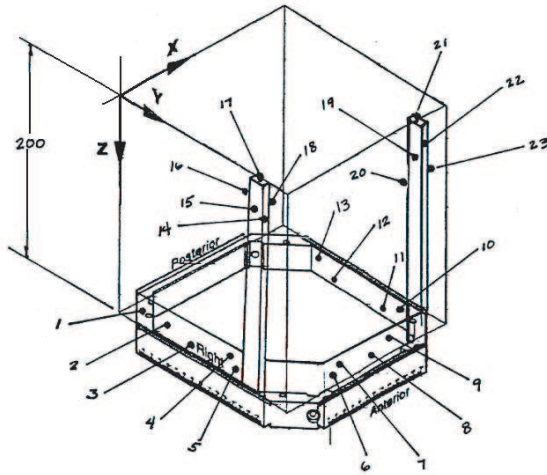


Fig. 2.3: Harvey Mudd Marker Caddy Design

2.5 Supporting Components

A host of supporting components are needed to facilitate the use of the marker systems. Some of these parts are: the micro-stage, micro-stage cart, wand and a regular digital camera system.

2.5.1 The Micro-Stage

The micro-stage is a fine alignment system capable of sub-millimeter fine alignment with three degrees of freedom. The degrees of freedom are the standard translations X,Y and Z. The micro-stage found flush on the table in fig 2.7, could be detached and mounted on a bracket (fig 2.6). Additionally, the micro-stage mounts using the bracket, directly on the patient bed used in the proton gantry at Loma Linda University Medical Center as in figure 2.9 and figure 2.10.

2.5.2 Micro-Stage Cart

Some of the experiments conducted in a lab setting required a patient bed in order to perform the course alignment. Since a patient bed is not available at California State University San Bernardino it was necessary to replace that capability

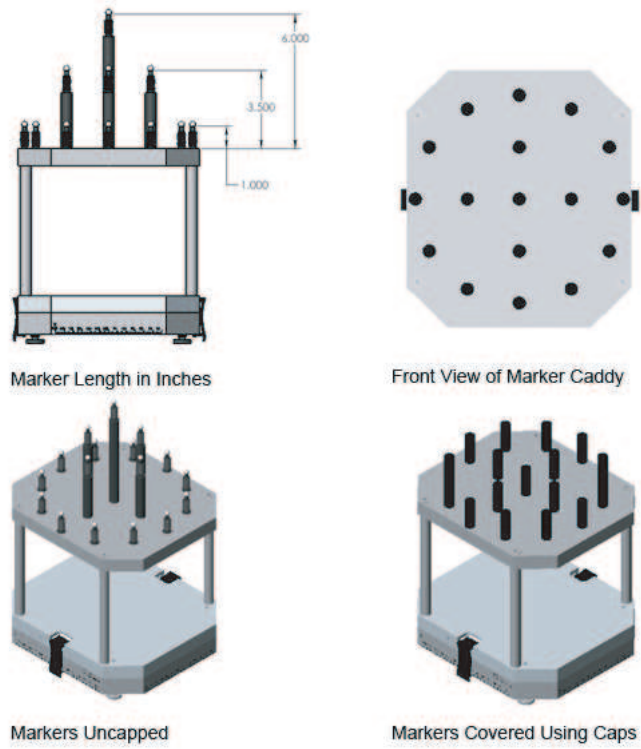


Fig. 2.4: New Caddy Design

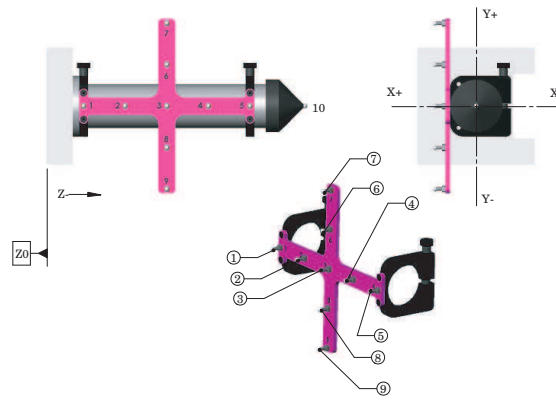


Fig. 2.5: Cone Cross Marker System

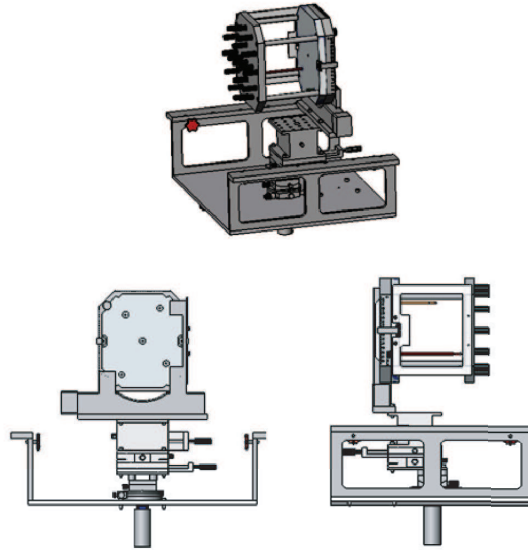


Fig. 2.6: Caddy Mounted on the Micro Stage with Bracket

with a similar (but manual) system. The Micro-stage (fig 2.6) mounts interchangeably on the cart (fig 2.7) or on the patient bed using a bracket as shown in figure 2.9.

2.5.3 L-Frame and Calibration Wand

The L-Frame is a marker set used at the static calibration procedure. Its purpose is to define the Vicon global coordinate system. The L-frame contains 4 markers shaped like the letter L. The first set of markers establishes the X coordinate and the other establishes the Y coordinate. The cross product of the two coordinate lines establishes the Z coordinate. The calibration wand is a small wand that contains two markers. The wand is used in the dynamic calibration process. The dynamic process (or calibration technique) was studied as one of the factors affecting the accuracy of the Vicon system (refer to chapter 3).

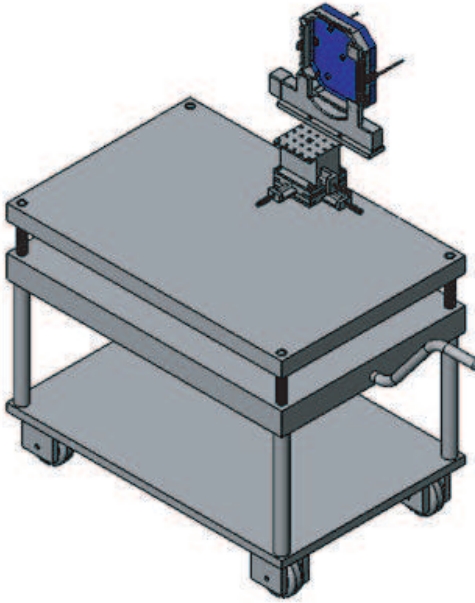


Fig. 2.7: Micro Stage Mounted on Specialized Cart

2.6 PACS System Setup

The main hardware components of the positioning and alignment control system (PACS) for functional proton radiosurgery are shown in photograph found in Figure 2.8. A more visible sketch of the components (excluding the cameras) can be found in figure 2.9. From the figures mentioned, we can see the caddy with the bracket mounted on the patient bed. We can also see the cross marker system attached to the proton nozzle to mark the position of the beam; The nozzle is collimated to the required beam diameter. The Vicon cameras can be seen behind the patient bed and approximately centered to the mid-point between the nozzle and the caddy. From the figures, we cannot see some of the other components including some of the support tools and computers but they are present behind the scene to connect all those systems together and run the alignment procedure.



Fig. 2.8: Experimental Setup with Main Hardware Components of the PACS.

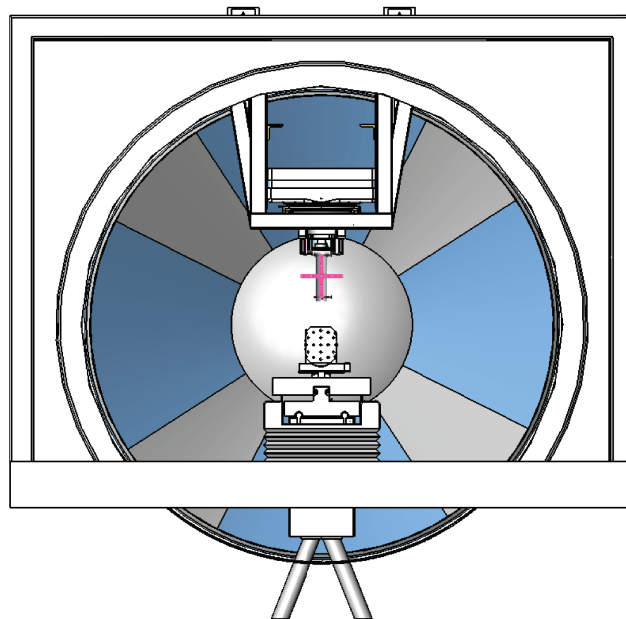


Fig. 2.9: Marker Systems in Gantry Setup

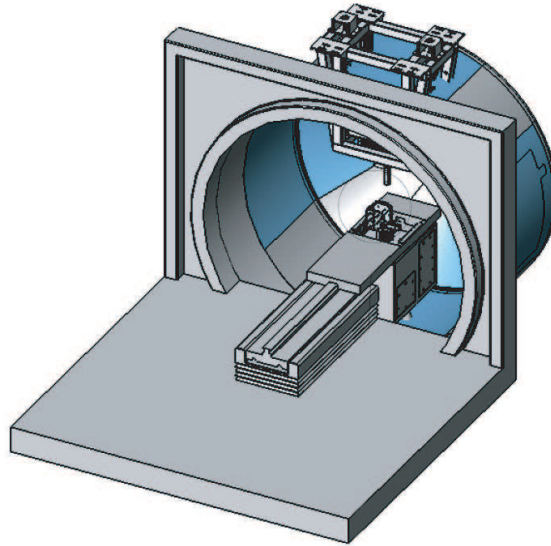


Fig. 2.10: Marker Caddy, Fine Alignment Stage and Holding Bracket in Gantry

2.7 PACS System Functional Description

After introducing all the hardware components of the PACS system, in this section we will focus on the the deployment of the system and the interaction between the sub systems and external systems that ultimately lead to the alignment procedure.

Figure 2.11 shows the deployment diagram for the PACS system. From the figure we can see the major components of the PACS system. The process starts with the Immobilization System (IS). A patient (animal at this stage) must be first immobilized using an immobilization frame (fiducial) fixed to the Leksell halo. The patient along with the fiducial will be sent to MRI for target localization from which we obtain the coordinates for the targets. The next system needed will be the OLS system.

The Optical Localization System is comprised of the Vicon cameras, the marker sets and all the other peripherals of the OLS. The main functionality of the OLS system is to localize the markers in 3D space so that we can locate the target in relation to the Leksell halo marker frame in the Vicon global coordinates. Steps involved in the OLS operation are system calibration at the beginning of a mea-

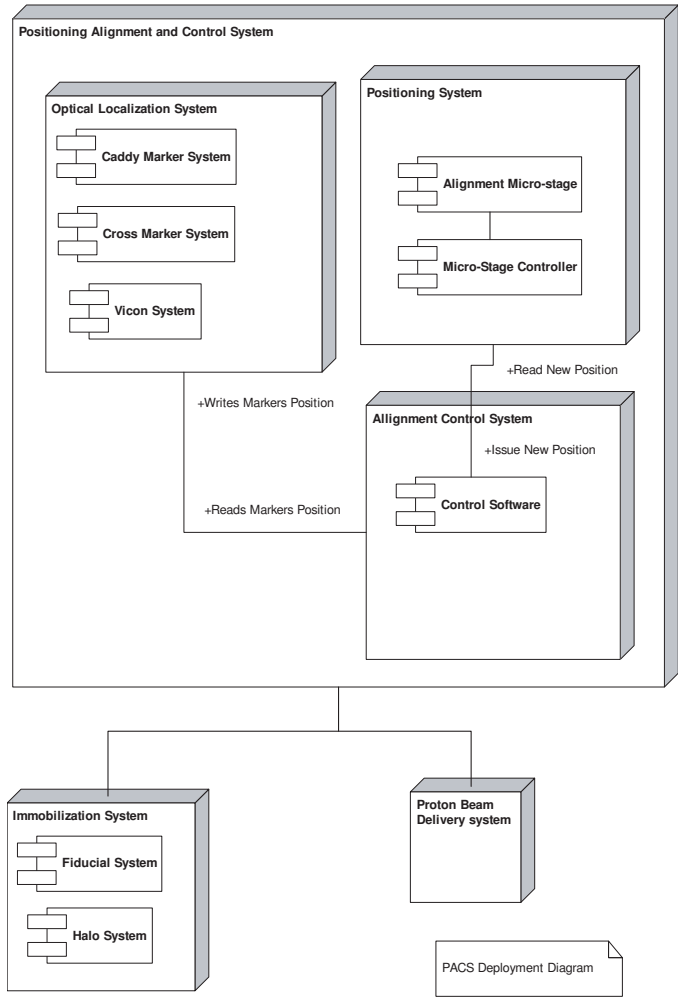


Fig. 2.11: PACS Deployment Diagram

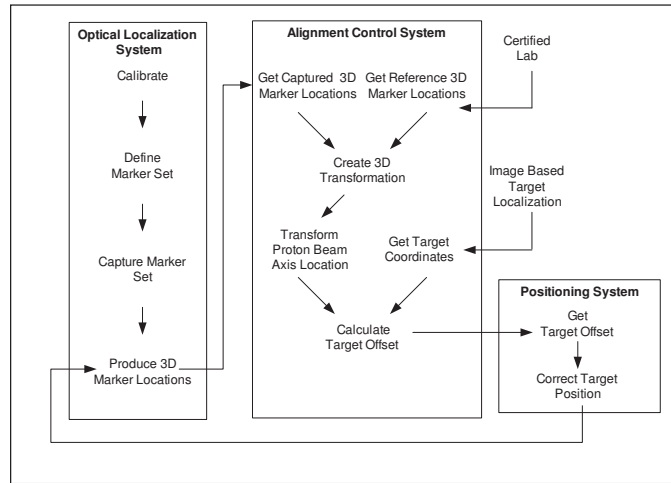


Fig. 2.12: Interaction Between the PACS System and Other Components

surement session, initial capture, and definition of marker sets for automatic marker recognition for subsequent marker captures. The location of the caddy markers are found and the locations of the cross markers are also found in the Vicon global coordinate system. The alignment control system takes the marker positions from the OLS and obtains the target location. After reading reference data, the ACS calculates a position correction for the caddy. The position correction is then taken by the Positioning System (PS) and the alignment is carried out. When the target is aligned within a certain tolerance, then the Proton Beam Delivery System would be asked to deliver beam.

2.8 Operation of the Alignment Control System

The alignment control system is one of the major parts developed and improved in this body of work. Figure 2.13 shows the flow chart for the ACS system.

From the figure we can see that the control system can be viewed as a continuous or a non-continuous model. One of the improvements on the system is directly visible which is the quality check prior to continuation of any calculation step. When all the quality measures are satisfied then the process continues through the steps. The system does not assume any number of targets or any number of alignment steps.

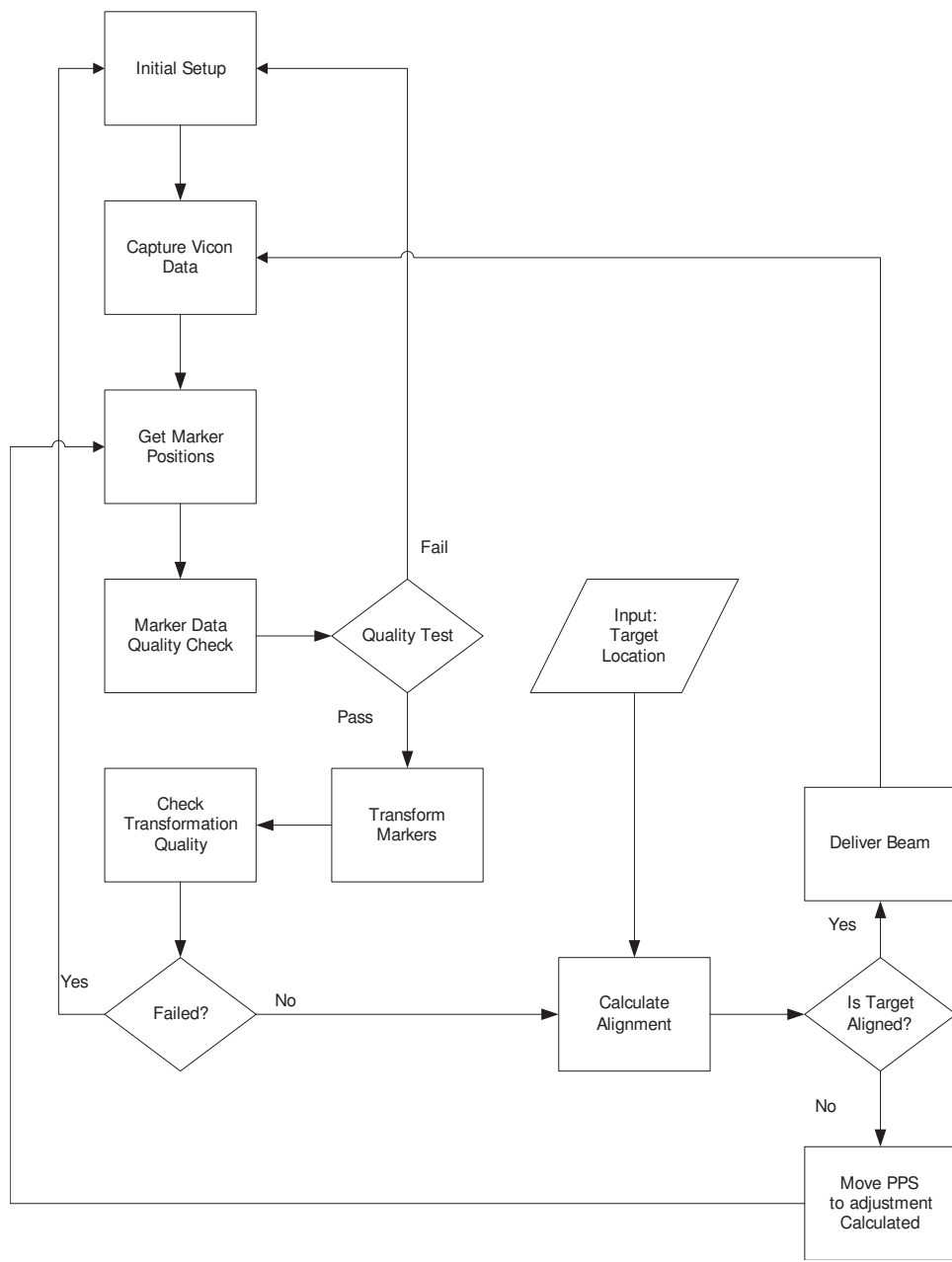


Fig. 2.13: Flow Chart of the PACS System

When all the quality tests pass and the target is determined to be aligned, then the beam is allowed to be delivered. The control process at the current stage is fully automated up to the point where a positioning is required (external to the control).

2.8.1 Stereotactic Transformation Algorithm

In order to align a proton beam to a target, one must be able to describe the target (very small) as a point, and the proton beam as a line. Furthermore, the target point and the beam line must be both described in the same coordinate system. To calculate the equation of the proton beam line in the stereotactic coordinate system we use the transformation algorithm described in appendix 7.2.5.

3. OLS SYSTEM CHARACTERIZATION

3.1 *Introduction*

The Vicon Camera System measures the position of retro reflective spherical markers in a right-handed global coordinate system that is defined at the time of the static calibration with the L-frame and calibrated during the dynamic calibration with the wand. The current system employs three digital cameras and software provided by Vicon. As this system is the central performing unit in the sequential alignment system for functional proton radiosurgery, it needed to be carefully characterized. This was done with a series of experiments performed between May and August of 2006.

3.2 *Purpose*

The experiments were designed to test overall accuracy, repeatability and reproducibility of marker position measurements. In particular, we wanted to determine the influence of the following experimental and confounding factors on the accuracy and precision of the marker position measurements:

- camera configuration
- calibration technique
- marker quality

3.3 Terminology

The following terms, common to metrology systems, will be used to characterize the Vicon Camera System:

- **Measurement Error:** The variability in the measurement observed due to the measurement process rather than the quantity measured. In the case of the marker system measurement, this means that we assume that the distances between the various markers is constant in time and, by itself, does not vary but the measurement of this distance varies due to errors introduced by the Vicon system.
- **Calibration:** A process for comparing actual reading to their known values in order to make adjustments so that the agreement between the two is improved. The Vicon system provides its own system calibration to properly scale the distance measurements and correct for lens distortions. In our measurements, an additional calibration of the distance scaling factor was introduced to improve the overall accuracy of the measurements.
- **Accuracy:** The total measurement variation including not only precision (see below) but also a systematic error (bias) between the average of measured values and the true value. A bias could be introduced, for example by using an inaccurate scaling factor or by an uncorrected geometric distortion of the camera images.
- **Precision:** Variability of a measurement process around its mean value (and not the true value). Precision may be further decomposed into short-term variation or repeatability (e.g., within one calibration) and long-term variation or reproducibility (e.g., between different calibrations)
- **Repeatability:** The component of precision that is the variability in the short term and occurs under highly controlled situations (e.g., same calibration, same experimental setup, same operator, etc.)

- **Reproducibility:** This is the total measurement precision in the long term occurring under different conditions (calibration, operator, ambient light etc.). Reproducibility includes the short term variation and is, therefore, equal to or worse than the repeatability.
- **Resolution:** Smallest interval between two measurements that can be meaningfully interpreted. Usually one quotes \pm one standard deviation of a representative sample of measurements as the resolution of a particular measurement. Thus, the resolution is closely related to the precision of a measurement.

3.4 *Independent Experimental Factors*

3.4.1 *Camera Configuration*

The three Vicon cameras were placed in a vertical equilateral triangle configuration and the camera plane was roughly parallel to the plane of the markers. Two individual camera configurations were tested within this scheme. The first configuration (see Figure 2.1), called “standard configuration” as it can be conveniently realized at the back of the proton gantry enclosure, featured an equilateral triangle of 104 cm side length. The cameras were oriented such that their central axes met at a single point (isocenter) which was located central between the two marker sets. The central axes formed equal angles of about 50 degrees with respect to each other. The distance of the isocenter, from the camera plane was 110 cm. The second camera configuration was an equilateral triangle with a side length of 177 cm. The central axes intersected at an angle of 90 degrees at a distance of 70 cm from the camera plane. Again, the isocenter was placed at the center point between the two marker sets. We hypothesized that this “orthogonal configuration”, although technically more difficult to realize, may lead to a higher degree of accuracy. For both camera configurations, the field of view of each camera at isocenter was 80 cm, ensuring that both marker sets were included in the field of view of each camera and resolved with identical resolution.

3.4.2 Calibration Technique

At the beginning of each measurement session, a static and dynamic system calibration was performed utilizing Vicon's automatic calibration algorithm Dynacal3. The static calibration captured four spherical markers (12 mm) with L-shaped arrangement rigidly attached to a frame. A least-square best fit line through three horizontal markers established the horizontal (X) axis of the Vicon reference system. The vertical (Y) axis was defined as the line perpendicular to the first line passing through the remaining single marker, and the longitudinal (Z) axis was defined by the cross product of unit vectors in X and Y direction. One should note that for calibration the L-frame was inserted in the holder that normally holds the stereotactic frame, thus making the Vicon system and stereotactic system axes parallel.

The dynamic calibration was performed by having the operator waving a 100-mm wand consisting of two spherical markers (12 mm) within the calibration volume, a cuboid of approximately 60 cm in side length. The exact distance between the centroids of the wand markers (98.923 mm), which is required for proper scaling, was measured by a certified inspection laboratory (Dimetrolab, Riverside, CA, USA). In addition, the distances between the individual markers of the L-frame were measured. These data were entered in the Calibration Reference Object (CRO) file of the Vicon software. In addition to the scaling factor, the dynamic calibration algorithm determined the position of the cameras relative to each other in space and the best-fit parameters of a linearization algorithm to correct for geometric lens distortions.

Each calibration produced three quality parameters: 1. The *camera residuals*, defined as the rms difference between the reconstructed marker image, based on the data of two cameras and projected back to the image of the third camera, and the marker image measured by the third camera; 2. the *wand visibility*, defined as the percentage of image frames with the wand seen by all three cameras; and 3. the *static reproducibility* defined as the relative accuracy (in percent) with which the inspected distances between static L-frame markers (CRO file entries) were reproduced. Camera residuals of less than 1 mm, wand visibility of 70% or better,

and static reproducibilities of 1% or better were accepted as indicators for a suitable calibration.

3.4.3 *Experimental Design and Data Analysis*

The goal of this performance study was to characterize the systematic and random measurement errors of the OLS under realistic measurement conditions and to identify the components in the variance of the error. The target marker set selected for this study consisted of 15 caddy markers distributed over an area of about 20 cm² in a plane parallel to the X-Y plane of the Vicon reference system.

The measurement accuracy and reproducibility of the system was studied using two endpoints: 1. the distances between each marker and the center of gravity (CG) of all other markers; and 2. the measured displacement of each marker after performing a prescribed shift in X, Y, or Z direction with micro-stages accurate to about 0.01 mm. Distances between CG and marker location in the stereotactic reference system were known from dimensional inspection to ± 0.025 mm. Differences between measured and nominal values were defined as distance and shift errors, respectively.

The performance study was organized into three individual experiments with camera configuration and calibration technique as the controlled experimental variables. The first experiment employed the camera configuration 1 (standard) and a calibration technique with random wand movements. The experiment consisted of three sessions, with 18 individual data captures (trials). The trials included a start position and six prescribed moves per X and Z axis covering a range of ± 15 mm and five moves per Y axis covering a range from -14 mm to +7 mm. Note that the Y axis had a more limited range of motion than the other two axes. The second experiment was identical in design but utilized camera configuration 2 (orthogonal).

The third experiment consisted of four sessions, each performed with camera configuration 1. For each session, a different calibration technique was used. The techniques differed with respect to the directionality of the wand movement: technique 1 used wand movement segments mostly perpendicular to the camera plane, technique

2 used movement segments mostly in vertical direction, and technique 3 used movement segments mostly in lateral direction; technique 4, which was also used in the first two experiments, combined random movements in all directions. Each session included 17 trials with a reference position and 16 prescribed shifts divided among the three axes with a range similar to that in the first two experiments.

Distance errors and shift errors were analyzed with respect to normality of their distributions using KS testing. For the first two experiments, grand means and standard deviations of marker session means were determined and compared using the Student t-test. For the third experiment, the marker session means and their standard deviations were compared with ANOVA. For each error type, variance and standard deviations were decomposed into marker, session, and trial effects using a linear statistical model of the form $y_{mst} = \eta + \varepsilon_m + \varepsilon_s + \varepsilon_t$, where y_{mst} is the measurement of marker m during trial t of session s , η is the population mean of all measurements, and ε_m , ε_s , and ε_t are random variables that describe the effect of marker and inter- and intra-session variability on the measurement, respectively. An ANOVA table was constructed to derive an estimate for the standard deviation of each parameter in the model. The 95% confidence intervals of the standard deviations were derived by performing 1,000 or 10,000 simulations with the sample variances of the ANOVA table [4]. Interactions between marker, session and trial effects were not considered in this analysis.

3.5 Results

3.5.1 Calibration Factors

We performed three experiments, the first two with three sessions for two different camera configurations using the same calibration technique, and the second with four sessions, one for each calibration technique using the same camera configuration. The three calibration parameters produced by the 10 sessions are summarized in Table 3.1. This shows that the mean and maximum residual camera errors were well below 1 mm. The visibility of the markers ranged from 68% to 98% and was

Exp.	Session	Camera (Mean \pm SD) (mm)	Res. Max Res. (mm)	Visibility (%)	Static Reprod. (%)
1	1	0.43 \pm 0.07	0.51	97	0.73
	2	0.47 \pm 0.10	0.56	97	1.08
	3	0.48 \pm 0.03	0.51	95	0.70
2	1	0.37 \pm 0.07	0.41	75	0.62
	2	0.26 \pm 0.02	0.28	68	0.49
	3	0.70 \pm 0.11	0.82	71	0.52
3	1	0.53 \pm 0.04	0.57	98	0.77
	2	0.54 \pm 0.07	0.60	97	0.72
	3	0.45 \pm 0.06	0.51	95	1.00
	4	0.44 \pm 0.05	0.49	96	1.00

Tab. 3.1: Calibration Parameters

typically above 90%. The static reproducibility ranged from 0.48% to 1.08% and was typically below 1%. No significant correlation between these factors and the session means of the distance and shift errors was found.

3.5.2 Distance Error

Distance errors were determined by calculating the difference between the distance of each marker from the CG of all remaining 14 markers and the corresponding distance measured by the dimensional metrology laboratory (DML).

During the first runs performed with the OLS, we noticed that the scaling factors determined by performing a linear regression of Vicon-measured CG distances against the DML CG distances, which ranged from 11.6 mm to 113.9 mm, were slightly above or below 1.0 (typically 1-2%). To make the absolute CG distance error independent of the magnitude of the CG distance, we henceforth determined the scaling factor for each measurement trial and used it to correct the CG distance accordingly. After this correction, no significant correlation was found between the error and the CG distance ($r = -0.15$, $p = 0.60$).

Exploration of the data of each session revealed no significant deviation of the distance error distribution from a normal distribution ($p > 0.05$, KS test). There was no significant correlation between the distance error and the size of the prescribed marker shift ($r = 0.44$, $p = 0.32$), nor were the session means of the distance error

Parameter	Level	Dist. (Mean \pm SD) (mm)	Error	Probability (p)
Camera Setup	Standard	0.088 \pm 0.155		0.89
	Orthogonal	0.083 \pm 0.213		
Calibration Tech- nique	1	0.120 \pm 0.163		0.71
	2	0.094 \pm 0.166		
	3	0.155 \pm 0.171		
	4	0.160 \pm 0.179		

Tab. 3.2: Mean Distance Errors

different when grouped with respect to shift axes X, Y, or Z ($p = 0.62$, one-way ANOVA).

Table 3.2 shows a comparison of the mean distance errors for the standard and the orthogonal camera setup (experiment 1) and the four calibration techniques (experiment 2). These values represent systematic measurement errors. Tabulated means are the averages across sessions and markers and the standard deviations are for the marker means. All means were of the order of 0.1 mm with no significant differences between the two camera configurations and the four calibration techniques. Standard deviations of the marker means ranged from 0.155 mm to 0.213 mm, representing the spread of systematic measurement errors between markers.

In order to study the variation of the individual measurement error, the standard deviations with 95% confidence intervals (in parentheses) of the distance measurement were obtained by ANOVA. These were 0.16 mm (0.12 mm, 0.25 mm) for the first experiment (camera configuration 1), 0.24 mm (0.19 mm, 0.36 mm) for the second experiment (camera configuration 2), and 0.17 mm (0.13 mm, 0.26 mm) for the third experiment (four calibration techniques), demonstrating an unexpected, significantly larger random measurement error for the orthogonal camera configuration ($p < 0.001$, F-test).

Figure 3.1 shows the decomposition of the standard deviation with respect to marker, session, and trial (intra-session) effects for the three experiments. It illustrates that the between-marker variation of the measurement error was the largest source of variation, followed by the inter-session variation, whereas the residual intra-

session variation was relatively small (standard deviation less than 0.05 mm). The inter-session standard deviation was significantly larger for camera configuration 2, explaining the larger overall standard deviation of this experiment. The use of different camera calibration techniques for each session (experiment 3) did not significantly increase the inter-session variability compared to the other two experiments, which used only one calibration technique.

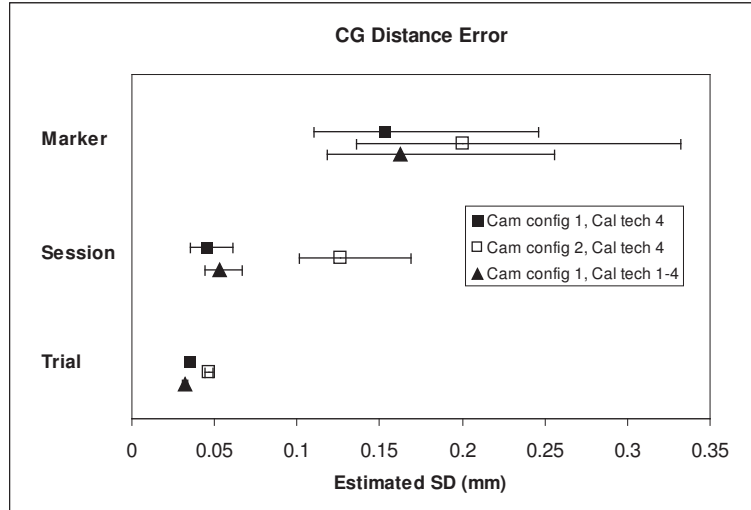


Fig. 3.1: Estimated Standard Deviation Components and 95% Confidence Intervals of the Distance Measurement.

3.5.3 Shift Error

Shift errors were determined by calculating the difference between prescribed shifts along the X, Y, or Z axis and measured shifts. For each session, shift measurements were corrected by the same scaling factor derived for CG distance data (see previous section).

Shift error distributions of individual sessions did not differ significantly from normal distributions ($p > 0.05$, KS test). There was a weak correlation between the shift error and the size of the prescribed marker shift: $\text{Shift Error (mm)} = -0.0312 + 0.00452 * \text{Shift(mm)}$, $r = 0.521$, $p < 0.0001$, probably due to residual scaling factor difference between measurements and micro-stage adjustments. Because the error

Parameter	Level	Dist. (Mean \pm SD) (mm)	Error	Probability (p)
Camera Setup	Standard	-0.036 \pm 0.018		0.85
	Orthogonal	-0.035 \pm 0.018		
Calibration Tech- nique	1	-0.032 \pm 0.021		0.075
	2	-0.024 \pm 0.014		
	3	-0.039 \pm 0.022		
	4	-0.024 \pm 0.014		

Tab. 3.3: Mean Shift Errors

introduced by this effect was very small, i.e., 4 micrometer per millimeter shift, no further correction to the shift error was made.

A small but significant difference of the mean shift error along the Y axis compared to the other two axes was found; the mean shift errors \pm standard errors for the X, Y, and Z axis were $-0.02 \text{ mm} \pm 0.004 \text{ mm}$, $-0.07 \text{ mm} \pm 0.004 \text{ mm}$, and $0.02 \text{ mm} \pm 0.004 \text{ mm}$, respectively ($p < 0.0001$, one-way ANOVA). This may be explained by the fact that the Y-axis micro-stage had to perform against the weight of stereotactic halo and target marker set.

Table 3.3 summarizes the mean shift errors and their standard deviations for the standard and the orthogonal camera setup (experiment 1) and the four calibration techniques (experiment 2). One should note that the mean shift errors were about three times and the standard deviations of the marker means about 10-times smaller than those for the distance errors.

The standard deviations with 95% confidence intervals (in parentheses) of the shift measurement were 0.09 mm (0.086 mm , 0.095 mm) for the first experiment (camera configuration 1), 0.089 mm (0.084 mm , 0.096 mm) for the second experiment (camera configuration 2), and 0.100 mm (0.096 mm , 0.104 mm) for the third experiment (four calibration techniques), demonstrating no significant dependence on camera setup and calibration technique ($p > 0.05$, F-test). Figure 3.2 shows the different components of the shift error standard deviation, illustrating that the contribution of variation between markers and sessions is very small in this case and practically all of the variation is due to intra-session variation. Also note that the lat-

ter is about two times larger than that of the distance error, which can be explained by the fact that the shift measurement consists of the difference between two marker coordinate measurements of about equal variance while the CG distance measurement involves the difference between a marker measurement and the average of 14 marker measurements (the CG location), which has a 14-times smaller variance than the individual marker measurement.

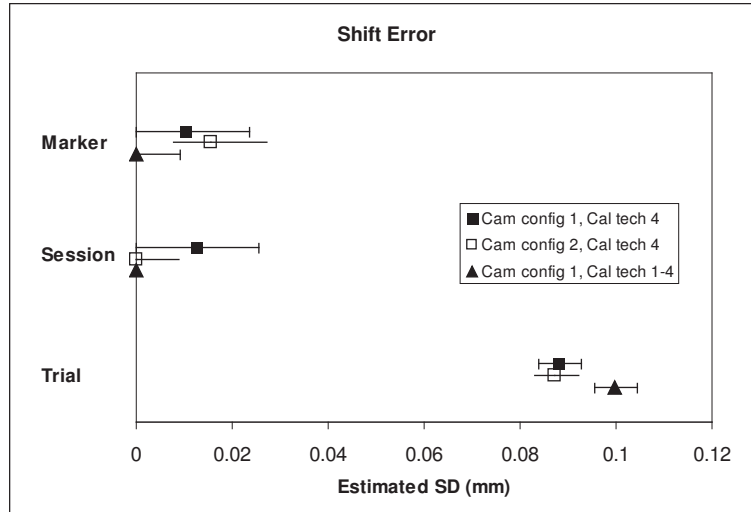


Fig. 3.2: Estimated Standard Deviation Components and 95% Confidence Intervals of the Shift Measurement. Negative Variances were Truncated to Zero.

3.6 Discussion and Conclusions

The goal of this investigation was to study the performance of the optoelectronic (optical) localization system for possible application in image-guided lesioning with narrow proton beams. With increasing capability for higher accuracy in animal and clinical brain lesioning procedures, due to better target localization, new techniques have to be developed that will allow application of sharp particle beams for this purpose.

Camera systems with active or passive markers attached to the human body have mostly been used for human movement studies in the past [7]-[13] and were only recently introduced to the field of image-guided radiotherapy and radiosurgery [11,

14]. The experience with these systems is limited and, in particular, no performance study of the Vicon system for this application has been published. In a review of available marker-based tracking systems, we have selected the Vicon system due to its real-time capability of automatic marker registration and its use of high-resolution cameras.

In this work, we studied two different endpoints that give different information on the performance of the system. The distance error is important for the accuracy and precision localizing the target and beam marker systems with respect to each other. Systematic and random system errors were of the order of 0.1 and 0.2 mm, respectively, which would be acceptable for the purpose of sub-millimetric alignment accuracy. We found that a significant source of the overall variation as well as systematic error was due to the markers themselves. This is probably related to the fact that the markers are made of a spherical ceramic core wrapped with retro-reflective tape, which introduces some variation in their spherical symmetry. A careful marker selection could potentially improve the OLS accuracy and reproducibility to better than 0.1 mm.

We found that the camera configuration with orthogonal intersection of the central axes had a significantly larger distance measurement uncertainty than the standard camera setup with about 50 degrees between the central camera axes. This unexpected result may be explained by the fact that the Vicon markers are incomplete spheres due to a flat part serving for marker attachment to their posts. With the standard camera arrangement, this part was practically invisible to the cameras, while for the orthogonal arrangement it was partially visible.

The second study endpoint, the shift error, is a measure of the accuracy and precision of spatial shifts with respect to a reference position. This is important for real-time tracking of small motions of the target and beam relative to each other. Overall, this error was about one magnitude smaller than the distance error. This can be attributed to the fact that this error is rather independent of the marker quality since the shift measurement only tracks relative changes in the position of the

same markers while the distance measurement involves the position of each marker relative to all other markers. Thus if the marker is perceived in the wrong location, this will affect its distance but not its shift measurement.

In addition to marker variability, both intra- and inter-session variability contribute to both distance and shift measurement errors. The intra-session error is probably due to random internal error sources, such as electronic noise and marker flickering. The inter-session errors could be related to the variability in manually calibrated measurement volume of the system. The intra-session error may be reduced with technical advances in marker recognition and low-noise electronics, or by adding additional cameras and decreasing the distance between cameras and markers. The inter-session error may be improved by standardizing the dynamic calibration technique with a robotic system.

In conclusion, this initial OLS performance study has shown that the Vicon system model 260 in combination with passive retro-reflective markers appears adequate for the stated purpose of monitoring functional proton lesioning procedures with sub-millimeter accuracy. The application accuracy of the integrated PACS, which depends on many additional factors, has yet to be tested.

3.6.1 Summary of Findings

In summary, the OLS (Vicon 260) system was tested for adequacy in sub-millimeter alignment applications. A series of experiments that included 2 experiments each including 3 calibrations and several trials was performed. The experiments were designed to test the accuracy, repeatability and reproducibility of marker positions. The end points of the experiments were to study the distance error and the marker shift error. The results showed that the different calibration techniques did not contribute a large error whereas the marker quality was the biggest contribution to errors. A larger error appeared when the second camera configuration was used but that error was still within an acceptable bound. The OLS system appeared to perform adequately for the purpose of sub-millimeter alignment using the standard

setup and current marker and camera systems.

4. IMPROVED CADDY DESIGN

4.1 Purpose

The purpose of this chapter is to report on the work done to improve the marker system used with the Optical Localization System in order to enhance its accuracy and functionality.

4.2 Theoretical Considerations

4.2.1 The Old Caddy Design

Before this body of work, a caddy was designed and implemented by the Harvey Mudd College (HMC) team in Claremont California. The caddy found in figure 2.3 consisted of a frame holding 23 markers. The HMC caddy was designed to maximize target visibility to the beam from all directions. The old caddy design however lacked many features that could make it more useful and had a few issues that needed a solution. Some of the issues the old caddy had are:

- **Crowding of markers:** The 23 markers on the caddy were placed in a way that maximizes a proton beam's entry angle; this caused the markers to be clustered together in a fashion that made marker visibility to the cameras limited. The visibility limitation made a few markers totally invisible to the camera system. Another issue was that markers who were very close to one another were recognized by the system as one marker at the centroid of the collection of miss-recognized markers.
- **Non-Symmetric Distribution of Markers:** As the markers were clustered, the markers were not distributed evenly over the volume of capture, which is

one of the factors in the quality of the measurement of that volume. The Vicon Cameras have their own inherent lens distortion, thus, placing the markers on the edge of the camera view rather than at evenly spaced intervals around the volume of capture increases the amount of error in recognizing the markers correctly.

- **Marker Configurations:** It is hard to cover or uncover the markers on the caddy in order to create particular marker configurations. It was necessary to create different marker configurations to test the theories in this thesis. The markers on the caddy did not have a way to hide them without the danger of breaking them.
- **Triangles:** The main theory in this body of work is that balanced and larger equilateral triangles should give more accuracy in the 3D transformation process. To test this theory it was required to create marker configurations that included large equilateral triangles using the caddy markers, and that was not available with the old caddy.
- **The phantom base:** The phantom base that houses measured targets had to be removed back and forth during the use to allow the caddy to register on the halo frame, which introduced human error.

4.2.2 *Requirements for a New Caddy*

As seen from section 4.2.1, the old caddy failed to fulfill some of the design goals of a usable caddy. To resolve the issues with the old caddy, a set of requirements were specified for a new caddy to be designed as part of this thesis work. The requirements for the new caddy were:

- The new caddy must have a configurable set of markers
- The markers on the new caddy should have a mechanism to cover and uncover them easily, without the big risk of breaking them.
- Markers on the new caddy should form a range of configurations ranging from small sharp triangles to large equilateral triangles for testing.

- The marker arrangements on the caddy should include two dimensional arrangements and three dimensional arrangements.
- The markers on the new caddy should be easily replaceable in case one gets damaged.
- The caddy itself should allow for a high visibility of target to the proton beam in addition of having markers with high visibility to the cameras.
- The caddy design should incorporate the peripherals of the old caddy including registration to the same Leksell halo and phantom base system.
- It was preferred that the caddy registers on the halo along with the phantom base without having to remove the phantom base during the caddy use in order to minimize the human error effect when replacing these parts.
- The new caddy design should fit a live animal module (frame) for future animal testing.

4.3 Engineering the New Caddy

4.3.1 Current Status of Design

Based on the requirements stated in section 4.2.2 a design effort for a new caddy took place. The new caddy design (figure 2.4) achieved all the requirements requested.

4.3.2 The Design Process

The design process of the new caddy started by estimating how the requirements would be satisfied. Since the requirements specified the need to use the existing registration system (halo), the design had to start from that point. The idea of the design was to attach the phantom base to the marker caddy firmly to create a device that would register on the halo. This idea achieved the goals of not having to remove the phantom base while using the caddy.

The caddy marker itself was realized as an aluminum plate with a set of screw threads that would hold the markers. The caddy plate itself is attached to the phantom base using 4 poles nearing 8 inch in length. The reflective markers where placed on aluminum rods that had threaded screws at the other end thus the markers are essentially screwed in place firmly on the marker plate.

The marker rods also had threads just behind the markers that would be used for matching plastic caps that have the same threads. Using the threaded marker method, the markers could be replaced and capped easily for protection and coverage. There where multiple lengths for the marker rods in order to realize a three dimensional configuration.

In order to achieve sharp and wide triangles with the markers, the marker set was modeled using 3D modeling software to achieve a good design. Twelve markers where eventually placed in a circle around the edge of the marker plate to form the large triangles and a set of five markers where placed in the center in a form of a small cross. The shape of the markers can be found in figure 2.4.

4.4 Experimental Verification of New Design and Selection of Best Marker Triangles

4.4.1 Purpose

The purpose of the triangle selection study was to determine the quality of the orthogonal stereotactic transformation for any triangular marker configuration possible with the new caddy design. Other purposes included ranking the triangles with respect to the root-mean-square (RMS) transformation error. furthermore, we needed to find characteristics of triangles that correlate with the RMS transformation error.

Note: The following method was used to calculate the RMS error:

1. generate all triangles
2. calculate stereotactic transformation for each triangle

3. apply transformation to all marker points including the selected triangle
4. calculate the error vector for each marker point
5. calculate sum of squared norms (SSN) for all error vectors
6. divide SSN by number of points and take the square root to obtain the RMS

4.4.2 *Triangle Study Hypothesis*

The hypothesis we had was that the RMS transformation error will decrease with increasing triangular area and increasing minimum triangle angle. The reason behind this theory is that the error in the OLS system is believed to be isotropic for the location of any particular marker and thus having a larger triangle will lead to a smaller relative error when processing the triangle through a transformation. Another reason we hypothesized is that smaller angles will lead to larger errors is the inherent structure of the transformation mathematics; When the angles between the vectors in a matrix are sharp the matrices become ill conditioned. Having ill conditioned matrices makes them prone to larger error due to slight perturbations.

4.4.3 *Method Outline*

We used all available Vicon system data captured between May and August, 2006 and studied the RMS error of the transformation for each triangle. The tests were designed and implemented using MATLAB software. The standard camera configuration was used for this study. The MATLAB software read in the data for three different sessions and all their trials (A session is an independent calibration). The software created all the possible triangles combinations for the 15 available markers used for this study. For each of the created triangles (455 in all), the triangle area was calculated, the smallest angle was determined and the transformation error was calculated. The values for the transformation error (RMS error) were averaged for the same triangle throughout the different sessions.

4.4.4 Results

Min Angle

You can find the plot of the min angle vs. the average RMS in figure 4.1. The angles are shown in radians and the RMS error shown is the average error for the same triangle throughout the different sessions. The error increases dramatically when the min angle approaches zero. The RMS error tends to be very small for a majority of the values and especially the ones with a larger minimum angle. To further show the difference between the errors, we can observe figure 4.2 which displays the same triangles but with error shown on a natural logarithmic scale. With the latter figure it is easier to see the trend; the larger the angle, the smaller the error is. We can also see that the difference between the two error extremes is several orders of magnitude.

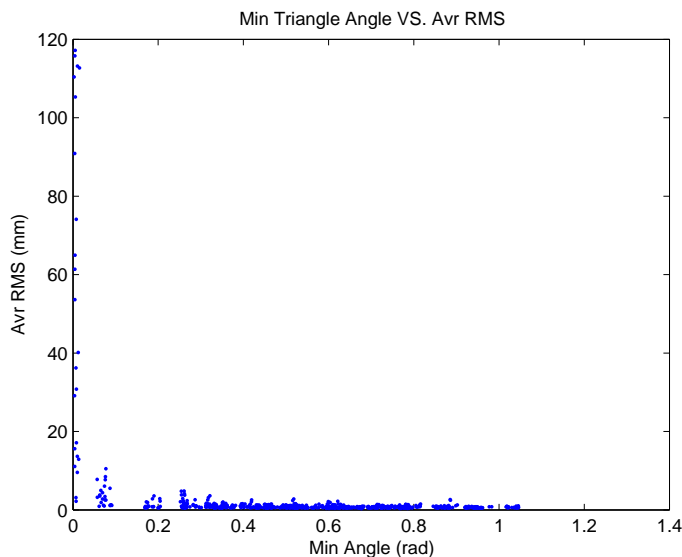


Fig. 4.1: Minimum Angle vs. Average Transformation RMS

Triangle Area

The results for the triangle area vs. average RMS look similar to the ones for min angle. From figure 4.3 we can quickly see that for most triangles where the

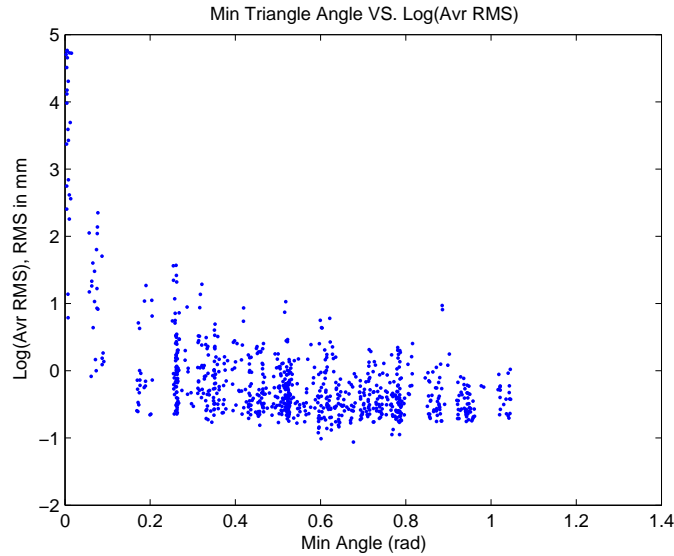


Fig. 4.2: Minimum Angle vs. Log(RMS)

area is above a certain threshold, the errors are smaller. For the triangles with an area below the threshold, the errors are extremely large and reached 120 mm. Using figure 4.4, we notice that the variation of error due to triangle area is a little larger than the variation due to angle change only. The trend however for triangle area can be easily seen, the larger the triangle area the smaller the average RMS error is. The majority of the triangles have an acceptable level of error but for the triangles on the smaller size the errors are too large to be acceptable for a transformation method.

4.4.5 Conclusions

The theory being tested was that the triangle area and min angle have a significant effect on the accuracy of the transformation of that triangle. The results show that the theory has merit. The intention is to use a few triangles to create the transformation between two coordinate systems. We can conclude that the triangle selection should be a very important step in the transformation; the reason is that one could choose one of those triangles that exhibit a large error, and use it without verification of its quality. For the intended application of sub-millimeter alignment,

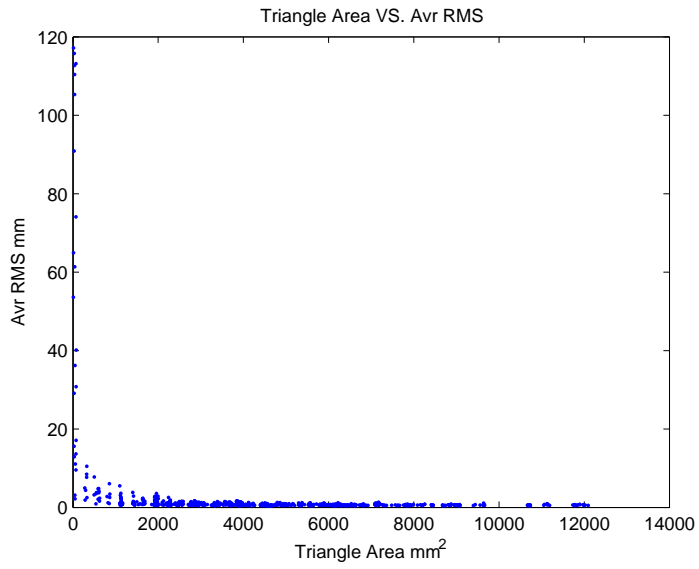


Fig. 4.3: Triangle Area vs. Average RMS

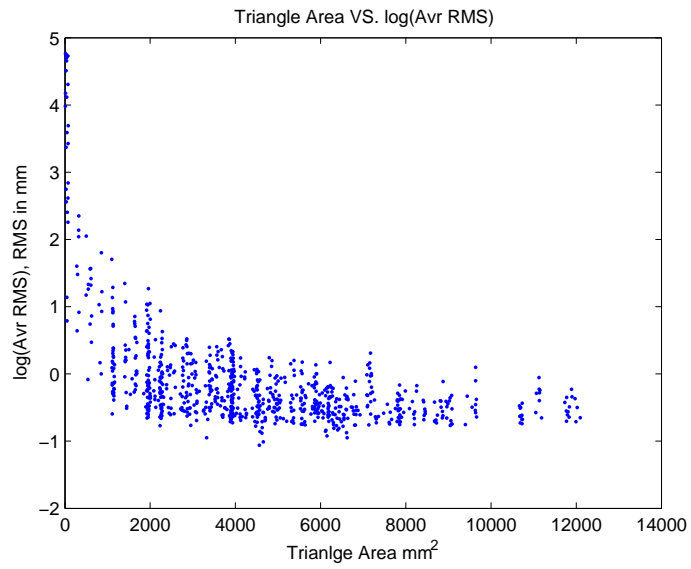


Fig. 4.4: Triangle Area vs. Log(RMS)

using a randomly selected triangle could be a hazard causing the alignment error to be significant thus this step is crucial.

4.5 *Summary of Improvements*

In summary, a triangle selection study was performed using the data sets obtained between May and Aug 2006. We tested the theory that the RMS transformation error will decrease with increasing triangular area and increasing minimum triangle angle. The results for the triangle area vs. average RMS look similar to the ones for min angle and they both give merit to the hypothesis. We can conclude that the triangle selection should be a very important step in the transformation method. The triangles selected for the transformation method should be of initial good quality. The same results are assumed to apply to the marker cross system.

5. REFINEMENT OF THE STEREOTACTIC TRANSFORMATION ALGORITHM

5.1 Purpose

The purpose of the refinement task was to step through the calculations done in the stereotactic transformation and correct any sources of numerical errors. The most significant improvements are described in the following few sections.

5.2 Triangles used in the Transformation

One of the improvements was to increase the number of triangles used to calculate the transformation matrix. The problem source is that the accuracy of the transformation matrix calculated using one triangle will be highly dependent on the accuracy of that particular triangle.

We solved that problem by using multiple triangles and averaging the rotation matrices produced by each triangle into an average rotation matrix.

5.3 Averaging of Rotation Matrices

In the previous section we introduced the use of an average rotation matrix. Initially this rotation matrix was averaged out using matrix addition and division by the number of matrices. The straightforward averaging was problematic because the resulting matrix is not necessarily a rotation matrix.

The initial solution for this problem was to use an analytical version of the Euler method for rotation matrices. In that method, a rotation matrix is calculated then the Euler angles are derived from the rotation matrix. After calculating the

Euler angles for several rotation matrices, the Euler angles were averaged out; the final rotation matrix was constructed using the averaged angles. This method still had problems as the angles in the Euler method are not necessarily in the same quadrant. To solve this last issue, we reverted to using the average of the cosines and sines of the angles instead of averaging the angles themselves. When we applied the Euler trigonometric averaging, the resulting rotation matrix was sometimes not a rotation matrix but with a very small perturbation away from one.

The last improvement on the averaging of the rotation matrices was to enforce the resulting average to be a rotation matrix. The way we accomplished that is by turning the Euler method into a numerical method and adding a cost constraint attached to a search function that maximized the cost of being away from a rotation matrix. The cost added function is considered a barrier function. A barrier function is a continuous function that is near infinity outside the feasible region and near 0 inside the feasible region. The feasible region is the region where the constraints are satisfied. A common barrier function for the region $[a, b]$ is $-c \log (x - a)(b - x)$

where c is adjusted to approximate an ideal barrier function. Typical ranges of c are 1 to .01.

The actual cost function we used in our application was:

$$-c \log \frac{1}{d^2} ((1 - d) - |M_{av}|)(|M_{av}| - (1 + d)) + 2 \log d$$

where $c = 1$ and $d = 10^{-4}$

5.4 Summary of Improvements

In summary, many of the sources of error in the transformation process were identified and corrected. The resulting process showed a higher level of accuracy and a lower transformation RMS error.

6. SOFTWARE IMPROVEMENTS AND DEVELOPMENT

6.1 Introduction

To improve the PACS system, many software packages had to be created or improved to make the system usable and efficient. The software tools inherited for this thesis work had many visible defects and some required calculations were done manually. As a result of this body of work, all the software inherited from SAPVS where rewritten from scratch. A collection of new software were added to the system most important of those is the alignment software. The following sections explore the different software improvements.

6.2 Camera Orientation Software

During the many experiments with camera configuration, it was determined necessary that we have a tool that aids the operator in calculating the camera angles that would make them exactly oriented at a point distant from the centroid of the triangle of the camera plane. In most cases that point referred to is the gantry isocenter. This software package is a GUI written in Visual Basic .NET. The software takes the height of each camera and the height of the isocenter as input; the user must also specify the distance to the iso center. After all the input is supplied, the software calculates the angle setting for each camera based on its height and distance and presents it to the user. A screen shot of the software interface can be found in figure 6.1. Many thanks to Mr. Pani Chakrapni for his support in writing this tool as his contribution was substantial.

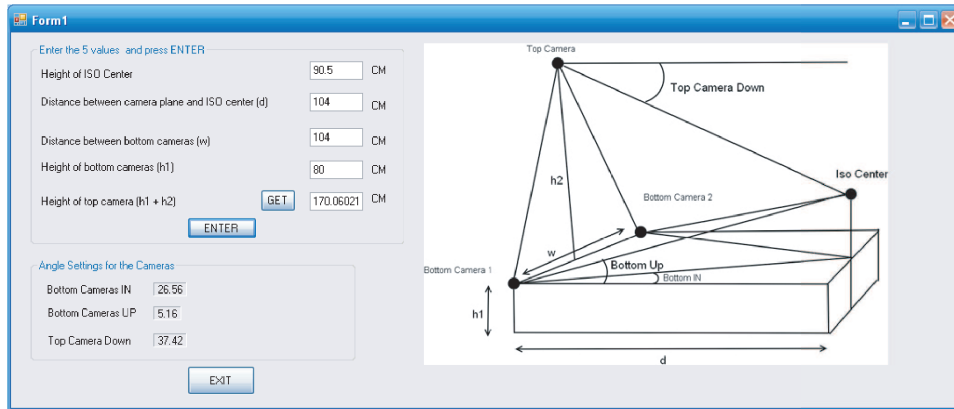


Fig. 6.1: Camera Position and Orientation Software.

6.3 Improving the Data Acquisition Process

In order to facilitate the data acquisition process an automated process to obtain the coordinates of the markers was needed. Previously this process was manual and required mundane work to obtain few data sets. To address this requirement a software plug-in was written to interface with the camera system.

The plug-in was written in C++ and utilized MFC¹ to create a static DLL that runs as a process from within the Vicon Workstation software. After the user captures a trial from within the Vicon Workstation, the user can execute that plug-in in the program's pipeline. The plug-in uses the captured c3d file as input and the output of the plug-in is a text file that contains a listing of all markers for all objects (marker systems). The listing contains the object name followed by the marker name followed by the X,Y and Z locations. The text file has a structure suitable for the transformation software to pick up and continue the transformation process. With this system, an automated solution now exists to generate the locations of the markers quickly and efficiently. The output of the plug-in is almost momentary.

¹ Microsoft Foundation Classes

6.4 *Improving the Image Processing Software*

In order to calculate the overall performance of the alignment system, an image based system was used to calculate the beam offset from the target. Targets with known coordinates are available for testing using the phantom base device (fig 2.6). A laser beam fitted inside the delivery nozzle was used to project light at the phantom base target. The shadow formed by the target marker and the laser are captured together using a digital camera. The offset of the center of the laser spot from the center of the target shadow is a direct indication of the alignment accuracy.

In order to process the laser spot/shadow images a software package was needed. In the course of this thesis the required software package was delivered. Figure 6.2 shows a screen shot of the image processing GUI. The Image processing GUI takes the raw images captured and processes them directly to produce the offsets between the two centers.

The following is the outline of the software algorithm:

- Read image from path pointed at by user.
- Threshold the image and convert to Black and White only.
- Clean the image noise by performing multiple progressive scans horizontally and vertically.
- Fill the laser spot completely and blacken the shadow area completely (image filling).
- Scan the image to determine outer bound of the laser spot.
- Create a contour around a large portion of the outer edge of the laser spot and arrange it as a matrix of X and Y points.
- Scan to find the shadow edge.
- Create a contour around a large portion of the shadow spot and arrange it as a matrix of X and Y points. The number of points matches the number of the points extracted for the outer spot.

- Solve the problem of finding the center of the circle from the matrix data using least square fitting.
- Calculating the Euclidean distance between the centers for the two circles.
- convert from pixel dimensions to millimeters by scaling the standard size of the laser spot (1 cm).
- Calculating and displaying the offset.
- Determining useful messages and displaying them on screen.
- Display the original image with the resulting circles and centers plotted on top of it with different colors.

The software package was implemented using MATLAB and was entirely written as a compilable GUI module that can run stand alone without MATLAB. To accomplish this the MATLAB compiler toolbox was utilized.

6.5 Implementation of a GUI based Alignment Package

One of the integral parts of the PACS alignment package is the alignment software. The alignment process for the SAPVS system was very mundane and required a good deal of user interaction. The actual alignment calculation was performed over a few steps some involving calculation of values using software tools like MATHCAD and required manual manipulation of the raw data in order to produce suitable data format. These conditions were to be corrected and thus a requirement for an automated tool was expressed early on and was stated as an objective of this thesis.

The alignment software was created and tested for the intended purpose. Figure 6.3 shows a screen shot of the alignment GUI. The software interface is designed for quick and repeated operation without too much intervention by the user (refer to figure 2.13). The user initially must select the reference files and the location of the data buffer (file) created by the plug-in. After those basic settings are selected, the

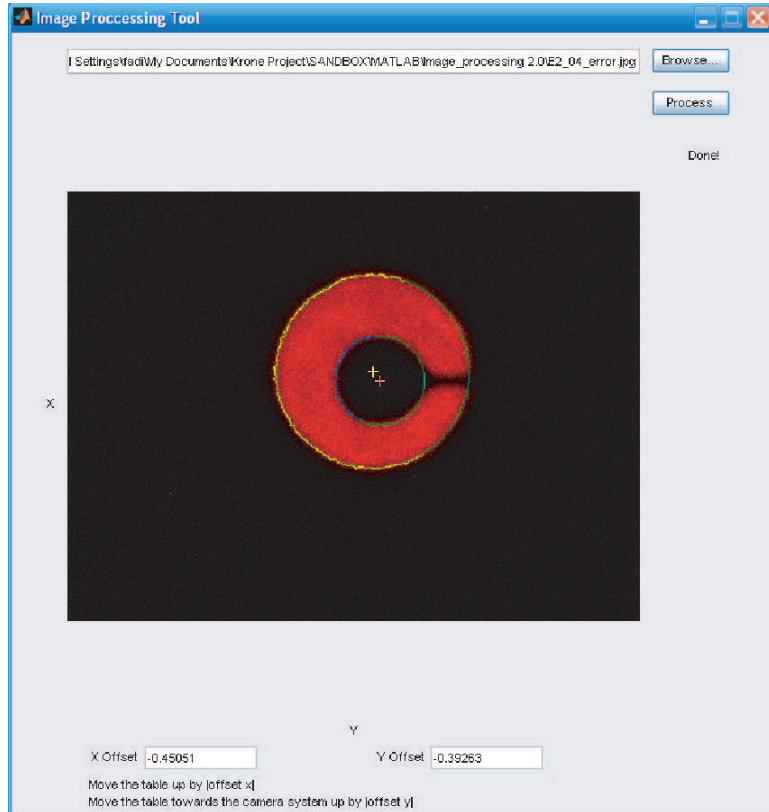


Fig. 6.2: Screen Capture for the Image Processing GUI.

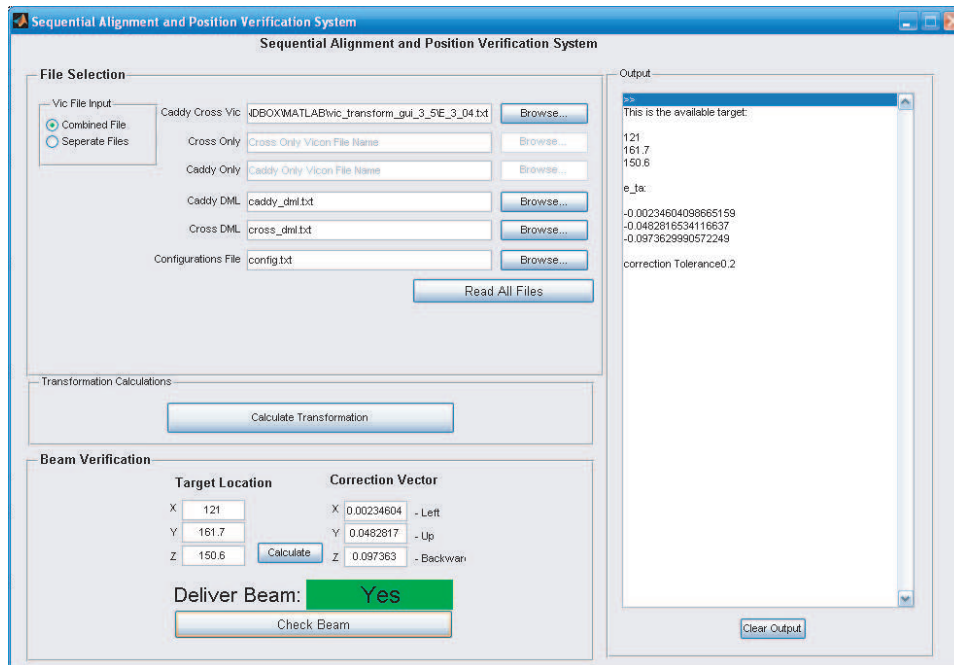


Fig. 6.3: Screen Capture for the Alignment GUI.

user can read all the files and create the transformation. The software reads all the needed files and calculates the transformation after checking the quality of the data. The quality of the transformation is then estimated and reported back to the user in the dialogue window. In the case where the quality is below a configurable value the dialogue window will display a red color background and a message is sent to the user stating which quality criteria where not met.

The alignment software is very easy to configure, as the software has a basic configuration file that can be modified based on the current use of the software. Some of the items that can be configured include the triangles selected for the transformation and the basic quality criteria. One other good feature of the software is that it remembers the files read and the target throughout the alignment process, thus the user can continue to align to the same target using the same settings until the alignment is achieved. An alignment check button is also available so that the user can verify the beam position to the set tolerance. The deliver beam display will remain red until the beam is on the target at which point it will turn green and the operator

will request beam.

6.6 *Summary of Software Improvements and Developments*

In Summary, many software tools and packages were developed for this thesis work. The most important software were described in this section in more detail and the following is a summary of those software.

The most important tool developed is the alignment software, this tool made the alignment process efficient and less error prone as the user intervention is minimized. This package is currently available with a non-continuous format but can be changed into a continuous mode as soon as the Vicon cameras are utilized in a real-time fashion. The other software was very useful in the course of this research and helped solve problems that would have taken a lot of time, especially the image processing tool and the camera alignment tool.

7. CONCLUSIONS AND FUTURE DIRECTION

7.1 *Conclusions*

Proton radiotherapy and radiosurgery are becoming more attractive options for the treatment of many ailments. The favorable features of protons over other ionizing radiation such as photon radiation will play a role in making proton based radiation the de facto standard in radiation oncology.

Sub-millimeter functional surgery is still not available with protons as of this writing. This thesis work is a step towards an optical based alignment and control system for sub-millimeter proton radiosurgery. The main product of this body of work is the PACS system. With the PACS system and similar systems, we believe that sub-millimeter accuracy is within reach and attainable in the near future.

In order to achieve sub-millimeter control over proton beams shooting through stereotactic defined targets, a set of hardware and software was integrated in a system named PACS. The PACS system contained an optical localization system and a patient positioning system. Both alignment and positioning system have sub-millimeter capabilities.

7.1.1 *Vicon Camera Performance*

In the previous efforts including the “SAPVS” system, a camera based localization system (VICON 260) was used. The camera system which is the major measurement tool available was never studied in terms of the many factors that can effect it’s overall accuracy. The different factors were examined in what was named the system characterization effort.

The system characterization effort was an attempt to quantify the precision

and accuracy of the Optical Localization System (OLS). The experiments focused on identifying the the significant sources of the errors in the system. The different confounding factors were examined including the calibration technique and the camera configurations. The major findings of the study done indicate that the main source of error is the quality of the individual markers. The calibration technique and camera configuration showed less effect on the overall accuracy of the system. Based on all the experiments and results, we have concluded that the optical localization system we tested will be adequate for sub-millimeter target localization.

7.1.2 *The Improved Caddy*

The caddy is a frame that holds a set of markers in space. The first caddy used in this research was designed by a team at Harvey Mudd College. The HMC design had pros and cons, but the cons of the device made it less useful for the research efforts in this thesis. A set of requirements for a new caddy were identified and a new caddy was designed. The newly designed caddy proved to be more efficient and useful for our purposes.

The markers on the new caddy were measured in an ISO certified laboratory to an accuracy better than 0.1 mm with respect to a commonly used frame (Leksell Halo). The triangles formed by the markers on the caddy are the essential components of the transformation math. The single most important theory that required testing in this thesis is the idea that certain triangles result in much more accurate transformations.

A triangle selection study was performed and aimed at identifying the triangles that produced the least amount of error in the transformation process. The theory tested was that that triangles with large area and near equilateral sides will perform much better than triangles with sharp angles and smaller areas. The conclusions from that study show that the difference between the two extremes is two orders of magnitude in difference for the RMS of the transformation error.

7.1.3 Rotational Transformation

While reviewing the mathematical methods used for the transformation and alignment methods, several issues were identified and needed to be corrected. One of the issues was that averaging of the rotation matrices for the different triangles was done incorrectly. This problem was fixed by introducing a method for averaging the matrices using Euler angles and averaging techniques that did a constrained search for the best solution. These methods showed higher accuracy with the final alignment of the beam to target in experimental settings. Other improvements to the mathematical procedure included using averaging of angles from different triangles using a new method that involved using sine and cosine based addition rather than straightforward addition of angles for the averaging. There were other smaller changes to the software that implemented the transformation to enhance its numerical accuracy. In general the transformation method was taken from version 2.6 up to version 3.5 with many revisions in between.

7.2 Future Direction

This body of work covered many areas and accomplished a good deal of results, yet there are still many things needed to achieve a reliable sub-millimeter alignment of proton beams to anatomical targets. Some of the suggestions and directions we have are found in the following.

7.2.1 Global System Performance

The PACS system has been tested in a lab setting with targets defined using phantoms measured at an inspection lab. The next step of testing would be to test the performance of the system on a phantom then a live animal in the hospital setting. This task can be achieved with the current PACS system but it requires a high level of coordination between teams taking care of different aspects of the task. A successful experiment with animals will showcase the capabilities of the system and will be

considered a breakthrough.

7.2.2 *Propagation of Error*

A study is needed to further explain the propagation of error throughout the system. A study is currently underway by Mr. Kevin Webster and a publication is expected soon. The results from a propagation of error study should be incorporated in future versions of the PACS system.

7.2.3 *Marker Systems*

From our studies we concluded that the marker quality was the most significant factor contributing to the RMS transformation error in the system. There should be an effort to minimize the effect of that factor in future work done. One of the suggestions is to create better markers using better materials and covering them with the retro-reflective material more evenly. Another way to improve the marker capture quality could be by using newer and improved Vicon cameras that take into consideration this effect.

7.2.4 *Vicon Cameras*

Using the Vicon cameras for the PACS system appeared to be adequate in terms of accuracy, but in terms of efficiency the system performs very poorly. The issues we found with the marker system are:

1. The calibration process is not uniform and determining the quality of the calibration is hard with just the residuals. We cannot determine which data set was used for the calibration and thus it was harder to relate the calibration technique with a particular wand pattern. The reason for this is that the Vicon system uses only 1000 frames for the calibration but the user does not know which 1000 frames it picks between the several thousand frames captured during the calibration. Note that for our calibration study we minimized the calibration time

to about 1000 frames to make sure that there will be a relation between the particular movement pattern and the captured data.

2. The Vicon cameras could also be improved in terms of their robustness; every time a person touches a camera, the entire calibration is thrown away and the whole process of calibration has to be redone.
3. The Vicon workstation software could use many improvements such as creating a means to capture the markers automatically for the same repeated subjects even on system restart. When the system is calibrated, the markers have to be labeled for identification. If for any reason a calibration is required, then those marker labels are gone and so are the subjects defined by them. It would be a nice feature if the cameras can anticipate the objects and figure out how to label them automatically or with little user intervention.

7.2.5 *The Cross Marker System*

The cross marker system is the system that locates the proton beam. This marker system was not improved during the course of this thesis work but should be improved in the near future. The lessons learned from the improved caddy design should be applied to the design of a new more reliable cross marker system.

APPENDIX A
STEREOTACTIC TRANSFORMATIONS FOR FUNCTIONAL PROTON
RADIOSURGERY

Note: *This Appendix is reproduced from the Master's thesis by Mr. Veysi Malkoc [8].*

Accurate stereotactic proton beam delivery for functional radiosurgery requires a mathematical transformation of coordinates from local coordinate systems (also referred to as dml), which change position in space during a treatment session, to a room-fixed global coordinate system, which is defined by the Vicon Motion Capture (vic) camera system.

In general, the axes of the different coordinate systems will not be parallel with respect to each other. Therefore, the coordinate transformations mapping each point of one reference system into another one involves both translations and rotations.

At least three linearly independent points, i.e., points that are not located on one straight line, with known coordinates in both reference systems are needed to calculate the equations for coordinate transformation between the two systems. The mathematical method to determine the coordinate transformation, which will be implemented in computer code for the Positioning and Alignment Control System (PACS) for functional proton radiosurgery, is described below. This Algorithm calculates the distance between the cone axis and a target based on orthogonal transformation from the cone reference system to the stereotactic reference system. For more information about what the caddy and cone are refer to chapter 2.

1.2 Mathematical Method to Compute the Transformation Between Local and Global Coordinate Systems

1.2.1 Outline of the Transformation Strategy

In the following discussion, the superscript^(g) indicates global coordinates and the superscript^(l) indicates local coordinates. In general, the coordinates of any point p_k^g in the global system is referred to as p_k^l in the local system. All coordinate systems

considered here are right handed.

Consider the triangle p_1^l, p_2^l, p_3^l in the local coordinate system, which is formed by three known markers (fig). Let $\mathbf{p}_1^l, \mathbf{p}_2^l$ and \mathbf{p}_3^l , denote the position vectors pointing from the origin of the local reference system to the central point of each marker.

Note that the lower case bold font indicates a vector and the upper case bold font indicate a matrix.

The corresponding position vectors to the triangle p_1^g, p_2^g, p_3^g in the global reference system are called $\mathbf{p}_1^g, \mathbf{p}_2^g$ and \mathbf{p}_3^g .

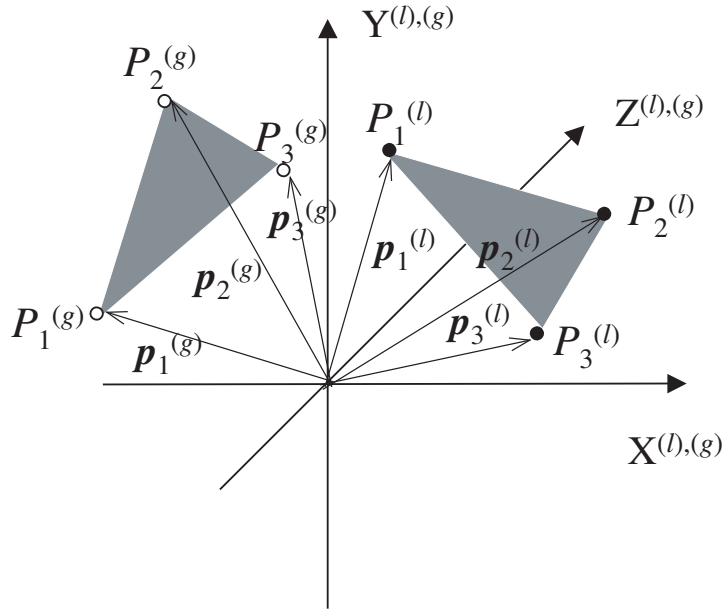


Fig. 1.1: Conceptual View of the Two Marker Sets in the Local and Global Reference Systems [8]

One may obtain the clearest perception of the rotations and translation involved in the coordinate transformation between the two reference system by assuming that the origins and axes of both coordinate systems coincide, and that the vectors $\mathbf{p}_1^l, \mathbf{p}_2^l, \mathbf{p}_3^l$ and $\mathbf{p}_1^g, \mathbf{p}_2^g, \mathbf{p}_3^g$ represent two different marker sets. Then the task to find a coordinate transformation between the two coordinate systems is identical to finding

the transformation that maps the local marker set onto the global marker set.

In general, the transformation equation, which maps corresponding l points onto g points, can be expressed as follows:

$$\mathbf{p}_n^g = \mathbf{M}_B \cdot \mathbf{M}_A \cdot \mathbf{p}_n^l + \mathbf{t} \quad (n = 1...3)$$

where \mathbf{M}_A and \mathbf{M}_B are 3x3 matrices representing proper rotations. The matrix \mathbf{M}_A corresponds to a rotation that makes the plane formed by the l marker set parallel to the plane formed by the g marker set. The matrix \mathbf{M}_B corresponds to an “in-plane” rotation, which aligns corresponding triangle sides with respect to each other. After performing these two rotations on the l triangle, the vector \mathbf{t} corrects for the residual translational difference between l points and corresponding g points.

1.2.2 Rotation of a Vector About a Non-collinear Vector

We now derive a useful equation for the matrix describing the rotation of a vector about another non-collinear vector. Consider a unit vector \mathbf{v} , which we want to rotate around a unit vector \mathbf{o} by an angle ϕ to form the vector \mathbf{v}' . Note that the angle θ between \mathbf{v} and \mathbf{o} is given by $\cos \theta = \mathbf{v} \cdot \mathbf{o}$.

We perform this rotation in a Cartesian coordinate system formed by the three orthogonal vectors: \mathbf{o} , $\mathbf{p} = \frac{(\mathbf{v} \times \mathbf{o})}{\sin \theta}$, and $\mathbf{q} = \frac{[\mathbf{o} \times (\mathbf{v} \times \mathbf{o})]}{\sin \theta}$, where the factor $\frac{1}{\sin \theta}$ is required to assure unit length. The rotated vector \mathbf{v}' can then be expressed in terms of these three unit vectors as follows:

$$\mathbf{v}' = (\mathbf{v} \cdot \mathbf{o})\mathbf{o} + \sin \theta \sin \phi \mathbf{p} + \sin \theta \cos \phi \mathbf{q}$$

By substituting the expressions for \mathbf{p} and \mathbf{q} in terms of \mathbf{o} and \mathbf{v} , and by taking into account that $\mathbf{o} \times (\mathbf{v} \times \mathbf{o}) = \mathbf{v} - \mathbf{o}(\mathbf{v} \cdot \mathbf{o})$, we find that

$$\mathbf{v}' = \mathbf{v} \cos \phi + \mathbf{o}(\mathbf{v} \cdot \mathbf{o})[1 - \cos \phi] + (\mathbf{v} \times \mathbf{o}) \sin \phi$$

This equation can also be expressed in matrix form as $\mathbf{v}' = \mathbf{M}\mathbf{v}$, where the

rotation matrix \mathbf{M} is explicitly given by

$$M = \begin{bmatrix} \cos(\Phi) + \mathbf{o}_1^2(1 - \cos(\Phi)) & \mathbf{o}_3 \sin(\Phi) + \mathbf{o}_1 \mathbf{o}_2(1 - \cos(\Phi)) & -\mathbf{o}_2 \sin(\Phi) + \mathbf{o}_1 \mathbf{o}_3(1 - \cos(\Phi)) \\ -\mathbf{o}_3 \sin(\Phi) + \mathbf{o}_1 \mathbf{o}_2(1 - \cos(\Phi)) & \cos(\Phi) + \mathbf{o}_2^2(1 - \cos(\Phi)) & -\mathbf{o}_2 \sin(\Phi) + \mathbf{o}_2 \mathbf{o}_3(1 - \cos(\Phi)) \\ -\mathbf{o}_2 \sin(\Phi) + \mathbf{o}_1 \mathbf{o}_3(1 - \cos(\Phi)) & -\mathbf{o}_1 \sin(\Phi) + \mathbf{o}_3 \mathbf{o}_2(1 - \cos(\Phi)) & \cos(\Phi) + \mathbf{o}_3^2(1 - \cos(\Phi)) \end{bmatrix}$$

1.3 Derivation of the Matrix M_A

To find the mathematical expression for the matrix M_A , which transforms the l triangle into one that is coplanar with the g triangle, we first determine the unit normal vector of the l triangle, $\mathbf{n}^{(l)}$, and the unit normal vector of the g triangle, $\mathbf{n}^{(g)}$. The two unit vectors can be calculated by forming and normalizing the vector products

$(\mathbf{p}_3^{(l)} - \mathbf{p}_1^{(l)}) \times (\mathbf{p}_2^{(l)} - \mathbf{p}_1^{(l)})$ and $(\mathbf{p}_3^{(g)} - \mathbf{p}_1^{(g)}) \times (\mathbf{p}_2^{(g)} - \mathbf{p}_1^{(g)})$, respectively (consult Fig 1.2a).

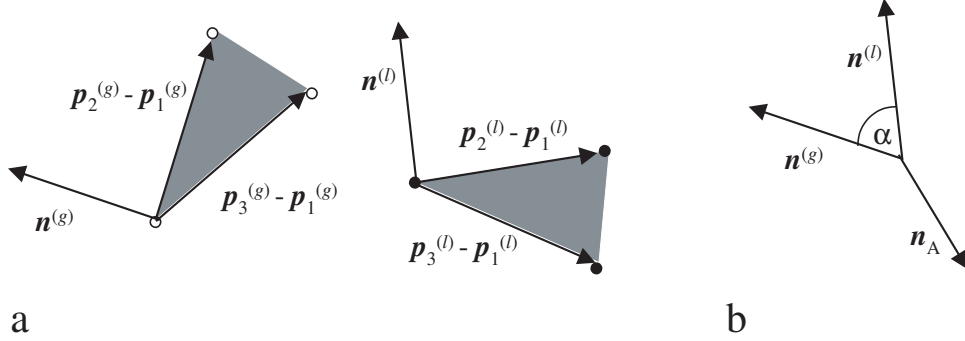


Fig. 1.2: (a) Definition of the Normal Vectors \mathbf{n}^l and \mathbf{n}^g , and (b) Rotation Performed by Matrix \mathbf{M}_A . [8]

The matrix M_A corresponds to a rotation of the vector unit $n^{(l)}$ about the orthogonal vector $\mathbf{n}_A = (\mathbf{n}^{(l)} \times \mathbf{n}^{(g)})$ by the angle α , where $\cos(\alpha) = \mathbf{n}^{(l)} \cdot \mathbf{n}^{(g)}$ (consult Fig 1.2b).

By normalizing the vector \mathbf{n}_A to $\mathbf{o}_A = \frac{\mathbf{n}_A}{\sin(\alpha)}$, and by using the expression for the rotation matrix M derived above, we obtain the following expression for the matrix M_A :

$$M_A = \begin{bmatrix} \cos(\alpha) + \mathbf{o}_{A1}^2(1 - \cos(\alpha)) & \mathbf{n}_{A3} + \mathbf{o}_{A1}\mathbf{o}_{A2}(1 - \cos(\alpha)) & -\mathbf{n}_{A2} \sin(\alpha) + \mathbf{o}_{A1}\mathbf{o}_{A3}(1 - \cos(\alpha)) \\ -\mathbf{n}_{A3} + \mathbf{o}_{A2}\mathbf{o}_{A1}(1 - \cos(\alpha)) & \cos(\alpha) + \mathbf{o}_{A2}^2(1 - \cos(\alpha)) & \mathbf{n}_{A1} + \mathbf{o}_{A2}\mathbf{o}_{A3}(1 - \cos(\alpha)) \\ \mathbf{n}_{A2} + \mathbf{o}_{A3}\mathbf{o}_{A1}(1 - \cos(\alpha)) & -\mathbf{n}_{A1} + \mathbf{o}_{A3}\mathbf{o}_{A2}(1 - \cos(\alpha)) & \cos(\alpha) + \mathbf{o}_{A3}^2(1 - \cos(\alpha)) \end{bmatrix}$$

Note that in this expression the terms $\mathbf{o}_{Ai} \sin(\alpha)$ have been replaced by \mathbf{n}_{Ai} ($i = 1 \dots 3$).

1.3.1 Derivation of the Matrix \mathbf{M}_B and the Vector \mathbf{t}

Multiplication of the local position vectors $\mathbf{p}_1^{(l)}$, $\mathbf{p}_2^{(l)}$, and $\mathbf{p}_3^{(l)}$ by the M_A matrix yields new vectors $\mathbf{p}'_1^{(l)}$, $\mathbf{p}'_2^{(l)}$, and $\mathbf{p}'_3^{(l)}$ which form a triangle that is now coplanar with that formed by the global position vectors $\mathbf{p}_1^{(g)}$, $\mathbf{p}_2^{(g)}$, and $\mathbf{p}_3^{(g)}$.

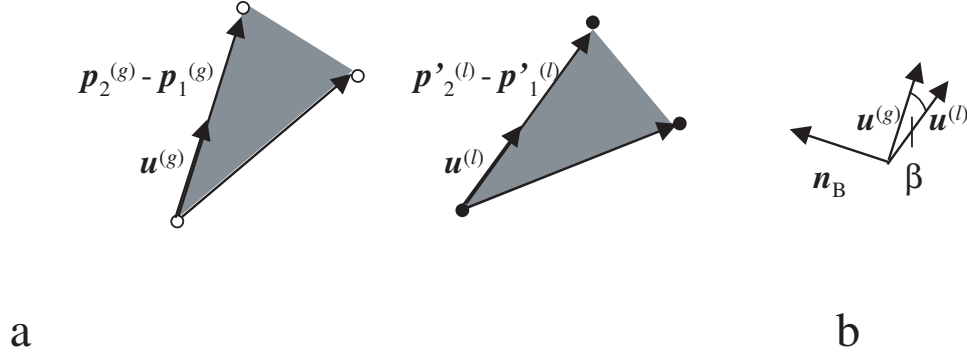


Fig. 1.3: (a) Definition of the Normal Vectors \mathbf{u}^l and \mathbf{u}^g , and (b) Rotation Performed by Matrix \mathbf{M}_B . [8]

To obtain the rotation matrix M_B , we normalize the triangle vectors $(\mathbf{p}'_2^{(l)} - \mathbf{p}'_1^{(l)})$, and $(\mathbf{p}_2^{(g)} - \mathbf{p}_1^{(g)})$, which yields the non-collinear unit vectors $\mathbf{u}^{(l)}$ and $\mathbf{u}^{(g)}$, respectively (Fig 1.3a).

The matrix that aligns unit vector $\mathbf{u}^{(l)}$ with unit vector $\mathbf{u}^{(g)}$ represents a rotation of the vector $\mathbf{u}^{(l)}$ about the orthogonal vector $\mathbf{n}_B = (\mathbf{u}^{(l)} \times \mathbf{u}^{(g)})$ by the angle β where $\cos(\beta) = (\mathbf{u}^{(l)} \cdot \mathbf{u}^{(g)})$ (Fig 1.3b). By normalizing the vector \mathbf{n}_B to $\mathbf{o}_B = \frac{\mathbf{n}_B}{\sin(\beta)}$ the matrix M_B can be expressed as:

$$M_B = \begin{bmatrix} \cos(\beta) + \mathbf{o}_{B1}^2(1 - \cos(\beta)) & \mathbf{n}_{B3} + \mathbf{o}_{B1}\mathbf{o}_{B2}(1 - \cos(\beta)) & -\mathbf{n}_{B2} \sin(\beta) + \mathbf{o}_{B1}\mathbf{o}_{B3}(1 - \cos(\beta)) \\ -\mathbf{n}_{B3} + \mathbf{o}_{B2}\mathbf{o}_{B1}(1 - \cos(\beta)) & \cos(\beta) + \mathbf{o}_{B2}^2(1 - \cos(\beta)) & \mathbf{n}_{B1} + \mathbf{o}_{B2}\mathbf{o}_{B3}(1 - \cos(\beta)) \\ \mathbf{n}_{B2} + \mathbf{o}_{B3}\mathbf{o}_{B1}(1 - \cos(\beta)) & -\mathbf{n}_{B1} + \mathbf{o}_{B3}\mathbf{o}_{B2}(1 - \cos(\beta)) & \cos(\beta) + \mathbf{o}_{B3}^2(1 - \cos(\beta)) \end{bmatrix}$$

Multiplication of the local position vectors $\mathbf{p}'_1^{(l)}$, $\mathbf{p}'_2^{(l)}$, and $\mathbf{p}'_3^{(l)}$ by matrix M_B yields new vectors $\mathbf{p}''_1^{(l)}$, $\mathbf{p}''_2^{(l)}$, and $\mathbf{p}''_3^{(l)}$, which makes the l triangle identical in orientation with respect to the g triangle. Finally we translate $\mathbf{p}''_1^{(l)}$ into $\mathbf{p}_1^{(g)}$ by adding the vector $t = \mathbf{p}_1^{(g)} - \mathbf{p}''_1^{(l)}$. If no systematic or random error is involved the triangles should now exactly superimpose.

The two rotations involved in the transformation can be combined into one rotation by calculating the matrix $M_{AB} = M_B \cdot M_A$. We then have

$\mathbf{v}^{(g)} = M_{AB} \cdot \mathbf{v}^{(l)} + \mathbf{t}$ for transformations of any vector \mathbf{v} from the local to the global coordinate system. Since the rotation matrix can be inverted, we can also transform in the opposite direction:

$\mathbf{v}^{(l)} = M_{AB}^{-1} \cdot (\mathbf{v}^{(g)} - \mathbf{t})$ This inverse transformation can be used to transform any vector from the global coordinate system into a local coordinate system.

1.4 Quality Check of the Transformation

Before proceeding to combine the transformations obtained for each triangle, we perform a quality check. This is done by applying the transformation to the points of each triangle in local coordinates and calculating the distance between the resulting points and the points in the global coordinate system.

first we get an average translation based on the three points of the transformed triangle:

$$t_1 = \mathbf{p}_1^{(g)} - \mathbf{p}''_1^{(l)} \quad t_2 = \mathbf{p}_2^{(g)} - \mathbf{p}''_2^{(l)} \quad t_3 = \mathbf{p}_3^{(g)} - \mathbf{p}''_3^{(l)}$$

$$t_{average} = \frac{t_1 + t_2 + t_3}{3}$$

then we can calculate the errors for each of the points

$$e_1 = |\mathbf{p}_1^{(g)} - M_{AB} \cdot \mathbf{p}_1^{(l)} - t_{average}| \quad e_2 = |\mathbf{p}_2^{(g)} - M_{AB} \cdot \mathbf{p}_2^{(l)} - t_{average}| \quad e_3 = |\mathbf{p}_3^{(g)} - M_{AB} \cdot \mathbf{p}_3^{(l)} - t_{average}|$$

The three individual point errors are then summed in square to calculate a combined error for each triangle:

$$e_{caddy} = \sqrt{(e_1)^2 + (e_2)^2 + (e_3)^2}$$

REFERENCES

- [1] Griffith A. Chipping in. *Scientific American*, 296(2):10,12, Feb 2007.
- [2] Richards G.M. et al. Linear accelerator radiosurgery for trigeminal neuralgia. *Neurosurgery*, 57(6):1193–200, Dec 2005.
- [3] T. Bergers et al. Restoring lost cognitive function. *IEEE Eng, Med Biol Mag.*, 24(5):30–44, Sep-Oct 2005.
- [4] A. Gelman. Analysis of variance - why is it more important than ever. *Ann. Statist.*, 33:1–53, 2005.
- [5] Lunsford L.D Kondziolka D. and Flickinger J.C. Stereotactic radiosurgery for the treatment of trigeminal neuralgia. *Clin. J. Pain*, 18(1):42–7, Jan-Feb 2002.
- [6] L. Leksell. The stereotaxic method and radiosurgery of the brain. *Acta Chir. Scand.*, 102:316–319, 1951.
- [7] V. Macellari. Costel: a computer peripheral remote sensing device for 3-dimensional monitoring of human motion. *Med. Biol. Eng.*, 21:311–318, 1983.
- [8] Veysi Malkoc. Sequential alignment and position verification system for functional proton radiosurgery. Master’s thesis, California State University San Bernardino, 2004.
- [9] Mahesh R. Neupane. Optimization of a sequential alignment verification and positioning system (savps) for proton radiosurgery. Master’s thesis, California State University San Bernardino, September 2005.
- [10] Wilson RR. Radiological use of fast protons. *Radiology*, 47:487–491, 1946.
- [11] W.A. Friedman et al. S.L. Meeks, F.J. Bova. Irled-based patient localization for linac radiosurgery. *Int. J. Radiat. Oncol. Biol. Phys.*, 41:433–439, 1998.

- [12] H. D. Suit. Protons to replace photons in external beam radiation therapy? *Clinical Oncology*, 15:S29–S31, 2003.
- [13] E. Nordh T. Josefsson and P.O. Eriksson. A flexible high-precision video system for digital recording of motor acts through lightweight reflex markers. *Comput. Methods Programs Biomed.*, 49:119–129, 1996.
- [14] J.M. Buatti et al. W.A. Tome, S.L. Meeks. A high-precision system for conformal intracranial radiotherapy. *Int. J. Radiat. Oncol. Biol. Phys.*, 47:1137–1143, 2000.

